

Whole Brain Susceptibility Mapping Using Harmonic Incompatibility Removal*

Chenglong Bao[†], Jae Kyu Choi[‡], and Bin Dong[§]

Abstract. Quantitative susceptibility mapping (QSM) aims to visualize the three dimensional susceptibility distribution by solving the field-to-source inverse problem using the phase data in magnetic resonance signal. However, the inverse problem is ill-posed since the Fourier transform of integral kernel has zeroes in the frequency domain. Although numerous regularization based models have been proposed to overcome this problem, the incompatibility in the field data has not received enough attention, which leads to deterioration of the recovery. In this paper, we show that the data acquisition process of QSM inherently generates a harmonic incompatibility in the measured local field. Based on such discovery, we propose a novel regularization based susceptibility reconstruction model with an additional sparsity based regularization term on the harmonic incompatibility. Numerical experiments show that the proposed method achieves better performance than the existing approaches.

Key words. Quantitative susceptibility mapping, magnetic resonance imaging, deconvolution, partial differential equation, harmonic incompatibility removal, (tight) wavelet frames, two system regularization

AMS subject classifications. 35R30, 42B20, 45E10, 65K10, 68U10, 90C90, 92C55

1. Introduction. Quantitative susceptibility mapping (QSM) [13] is a novel imaging technique that visualizes the magnetic susceptibility distribution from the measured field data associated with magnetization $\mathbf{M} = (M_1, M_2, M_3)$ induced in the body by an MR scanner. The magnetic susceptibility χ is an intrinsic property of the material which relates \mathbf{M} and the magnetic field $\mathbf{H} = (H_1, H_2, H_3)$ through $\mathbf{M} = \chi\mathbf{H}$ [45]. As physiological and/or pathological processes alter tissues' magnetic susceptibilities, QSM has been widely applied in biomedical image analysis [45]. Applications include demyelination, inflammation, and iron overload in multiple sclerosis [8], neurodegeneration and iron overload in Alzheimer's disease [1], Huntington's disease [50], changes in metabolic oxygen consumption [25], hemorrhage including microhemorrhage and blood degradation [28], bone mineralization [14], drug delivery using magnetic nanocarriers [34].

QSM uses the phase data of a complex gradient echo (GRE) signal as the phase linearly increases with respect to the field perturbation induced by the magnetic susceptibility distribution in an MR scanner [52]. More concretely, assume that an object is placed in an MR scanner with the main static magnetic field $\mathbf{B}_0 = (0, 0, B_0)$ where B_0 is a positive constant. Then, for any $\mathbf{x} \in \mathbb{R}^3$, the observed complex GRE signal $I(\mathbf{x}, TE)$ at an echo time TE sec is modeled as

$$I(\mathbf{x}, TE) = m(\mathbf{x}) \exp \{-i(b(\mathbf{x})\omega_0 B_0 TE + \theta_0(\mathbf{x}))\}, \quad (1.1)$$

*Submitted to the editors DATE.

Funding: The research of the third author is supported by NSFC grant 11831002.

[†]Yau Mathematical Sciences Center, Tsinghua University, Beijing, 100084 China, (clbao@math.tsinghua.edu.cn).

[‡]Corresponding Author. School of Mathematical Sciences, Tongji University, Shanghai, 200092 China, (jay-cjk@tongji.edu.cn).

[§]Beijing International Center for Mathematical Research and Laboratory for Biomedical Image Analysis Beijing Institute of Big Data Research, Peking University, Beijing, 100871 China, (dongbin@math.pku.edu.cn).

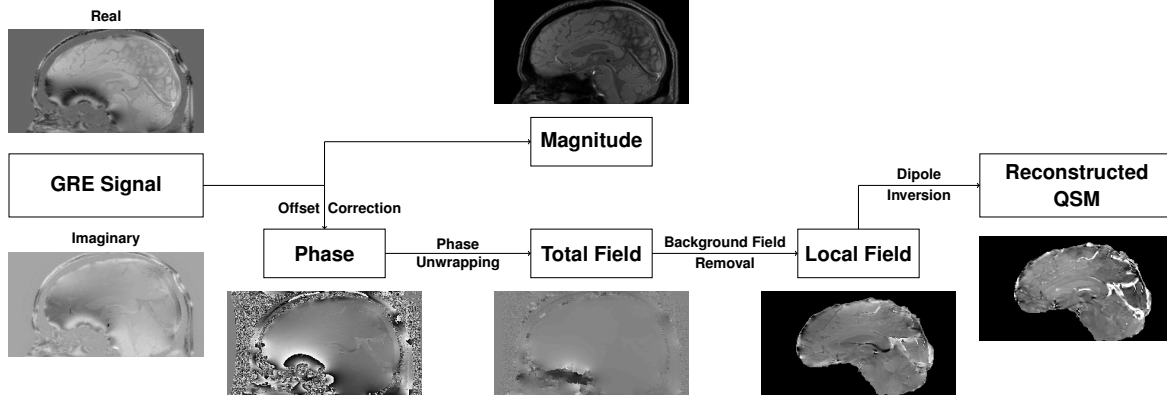


Figure 1. Schematic diagram of QSM reconstruction process.

36 where $\omega_0 = 42.577\text{MHz/T}$ is the proton gyromagnetic ratio, b is the total field induced by the
 37 susceptibility distribution in an MR scanner, and θ_0 is the coil sensitivity dependent phase
 38 offset. The magnitude image $m(\mathbf{x})$ in (1.1) is proportional to the proton density [52], and the
 39 phase $\theta(\mathbf{x})$ in $I(\mathbf{x}, TE)$ is written as

$$40 \quad \theta(\mathbf{x}) = b(\mathbf{x})\omega_0 B_0 TE + \theta_0(\mathbf{x}). \quad (1.2)$$

42 Based on the observations $\theta(\mathbf{x})$, QSM aims at visualizing the susceptibility distribution $\chi(\mathbf{x})$
 43 in the region of interests (ROI) Ω which occupies the water and brain tissues. Note that the
 44 ROI Ω can be readily determined by $I(\mathbf{x}, TE)$ (and thus by $m(\mathbf{x})$) as $m(\mathbf{x}) = |I(\mathbf{x}, TE)| \approx 0$
 45 whenever $\mathbf{x} \notin \Omega$ [30, 44, 52]. The standard QSM consists of the following four steps: offset
 46 correction, phase unwrapping, background field removal and dipole inversion (see Figure 1 for
 47 the overview of the process). The first three steps extract the local field b_l that is contained in
 48 the total field b : the offset correction removes/corrects $\theta_0(\mathbf{x})$ from $\theta(\mathbf{x})$ to obtain $b(\mathbf{x})\omega_0 B_0 TE$
 49 (the offset corrected phase) lying in $(-\pi, \pi]$; the phase unwrapping removes the artificial jumps
 50 in the offset corrected phase when estimating the total field b ; the background field removal
 51 eliminates the field induced by the susceptibility outside Ω such as skulls and nasal cavity.
 52 Interested readers may refer to [24, 44, 52] and references therein for more details.

53 Given the local field b_l , the dipole inversion recovers the susceptibility distribution χ in Ω
 54 by solving the following convolution relation [31, 32, 33]:

$$55 \quad b_l(\mathbf{x}) = \text{pv} \int_{\Omega} d(\mathbf{x} - \mathbf{y})\chi(\mathbf{y})d\mathbf{y}, \quad (1.3)$$

57 where pv denotes the principal value [48] of the singular integral with the kernel d :

$$58 \quad d(\mathbf{x}) = \frac{2x_3^2 - x_1^2 - x_2^2}{4\pi|\mathbf{x}|^5}.$$

60 In the frequency domain, (1.3) reads

$$61 \quad \mathcal{F}(b_l)(\boldsymbol{\xi}) = \mathcal{D}(\boldsymbol{\xi})\mathcal{F}(\chi)(\boldsymbol{\xi}) = \left(\frac{1}{3} - \frac{\xi_3^2}{|\boldsymbol{\xi}|^2}\right)\mathcal{F}(\chi)(\boldsymbol{\xi}) \quad (1.4)$$

62

63 where $\mathcal{D} = \mathcal{F}(d)$ is the Fourier transform of d and $\mathcal{D}(\mathbf{0}) = 0$ by the definition of pv [13, 24].
 64 From (1.4), it is easy to see that recovering the susceptibility distribution χ is ill-posed as
 65 $\mathcal{D} = 0$ on the critical manifold $\Gamma_0 = \{\boldsymbol{\xi} \in \mathbb{R}^3 : \xi_1^2 + \xi_2^2 - 2\xi_3^2 = 0\}$. This ill-posedness leads to
 66 the streaking artifacts unless the data b_l satisfies a proper compatibility condition [9].

67 **1.1. Existing QSM Reconstruction Methods.** In the literature, various QSM reconstruc-
 68 tion methods have been explored to deal with the ill-posed nature of the inverse problem (1.4).
 69 Early attempts mainly focus on the direct methods based on the modification of (1.4) near
 70 Γ_0 [27]. One benchmark method, called the truncated K-space division (TKD) [47], finds the
 71 approximate solution to (1.4) via:

$$72 \quad \chi_h = \mathcal{F}^{-1}(\mathcal{X}_h), \quad \text{where } \mathcal{X}_h(\boldsymbol{\xi}) = \frac{\text{sign}(\mathcal{D}(\boldsymbol{\xi}))}{\max\{|\mathcal{D}(\boldsymbol{\xi})|, \hbar\}} \mathcal{F}(b_l)(\boldsymbol{\xi}) \quad (1.5)$$

74 with a threshold level $\hbar > 0$. Another method recovers χ via solving the following Tikhonov
 75 regularization [29]:

$$76 \quad \min_{\chi} \frac{1}{2} \|A\chi - b_l\|_2^2 + \varepsilon \|\chi\|_2^2 \quad (1.6)$$

78 where $\varepsilon > 0$ and A denotes the forward operator that is obtained by discretizing the kernel \mathcal{D} .
 79 Recently, some other direct methods are proposed, e.g. the iterative susceptibility weighted
 80 imaging and susceptibility mapping [49], the analytic continuation [39] and so on. Even though
 81 these direct methods are simple to implement, they can introduce additional artifacts due to
 82 the modification of $1/\mathcal{D}$ near Γ_0 in the frequency domain [9, 27, 40].

83 In recent years, the regularization based methods have been proposed and show the supe-
 84 rior performance over the direct method [27, 51]. Mathematically, it is formulated as solving
 85 the minimization problem:

$$86 \quad \min_{\chi} F(b_l|\chi) + R(\chi), \quad (1.7)$$

88 where $F(b_l|\chi)$ denotes the data fidelity term and $R(\chi)$ is the regularization term which most-
 89 ly promotes the sparse approximation of χ under some linear transformation such as total
 90 variation and wavelet frames. According to the choices of $F(b_l|\chi)$, the regularization based
 91 methods can be classified into the *integral approaches* and the *differential approaches* [27].
 92 The most widely used integral approaches are based on the convolution relation (1.3). For
 93 example, $F(b_l|\chi) = \frac{1}{2} \|A\chi - b_l\|_2^2$ when the data is corrupted by a white Gaussian noise. Even
 94 though the integral approach is capable of suppressing streaking artifacts, it is empirically
 95 reported in [27] that the reconstructed image can contain the shadow artifacts in the region
 96 of piecewise constant susceptibility. The differential approaches are based on the following
 97 partial differential equation (PDE)

$$98 \quad -\Delta b_l(\mathbf{x}) = P(D)\chi(\mathbf{x}) = \left(-\frac{1}{3}\Delta + \frac{\partial^2}{\partial x_3^2} \right) \chi(\mathbf{x}) \quad \mathbf{x} \in \Omega \quad (1.8)$$

100 which is derived from the Maxwell's equation [23, 45]. In this case, one typical fidelity term
 101 is $F(b_l|\chi) = \frac{1}{2} \|P(D)\chi + \Delta b_l\|_2^2$ by considering $-\Delta b_l$ as a measurement. Compared with the

102 integral approach, the differential approach is able to restore susceptibility image with less
 103 shadow artifacts. However, the noise in the data can be amplified by $-\Delta$, which leads to the
 104 streaking artifacts [52]. In [27], the differential approach is implemented by incorporating the
 105 spherical mean value (SMV) filter S_r with a radius $r > 0$ [30] into the integral approach:

$$106 \quad \min_{\chi} \frac{1}{2} \|S_r(A\chi - b_l)\|_2^2 + R(\chi). \quad (1.9)$$

108 Since the implementation of S_r causes the erosion of Ω according to the choice of r , the loss of
 109 anatomical information near $\partial\Omega$ is inevitable at the cost of the shadow artifact removal [27].

110 **1.2. Motivations and Contributions of Our Approach.** Even though the equations (1.3)
 111 and (1.8) are known to be equivalent [9, 27, 40], it is observed that the local field b_l defined
 112 as (1.3) is a particular solution of the PDE (1.8). Whenever the data acquisition is based on
 113 the PDE (1.8), the measured local field data will be written as the superposition of b_l in (1.3)
 114 and the ambiguity of $-\Delta$, which will be referred as the *harmonic incompatibility*. Therefore,
 115 there is a need to identify/remove the harmonic incompatibility from the measured local field
 116 data for better reconstruction results as it is smooth, analytic and satisfies the mean value
 117 property in an open set [19], which are different from the noise properties.

118 It is noted that the background field removal aims at obtaining the local field b_l via solving
 119 a Poisson equation with certain boundary condition as the background field is harmonic in
 120 Ω [30, 43, 52, 57]. In this case, the measured local field b_l is represented by the Green's
 121 function associated with the boundary condition [9]. Thus, it is inevitable that b_l contains the
 122 incompatibility associated with the imposed boundary condition. In this paper, we investigate
 123 the incompatibility of the local field data in QSM and establish that this incompatibility
 124 consists of two harmonic functions inside and outside Ω respectively, and its (distributional)
 125 Laplacian defines a surface measure on $\partial\Omega$ (see Theorem 2.2 for details and Figures 2 to 5
 126 for illustrations). Therefore, we can establish a new forward model in QSM by taking this
 127 harmonic incompatibility into account.

128 Based on this discovery, we impose a constraint on harmonic incompatibility term in sus-
 129 ceptibility reconstruction model. Since our theoretical results suggest that the incompatibility
 130 is harmonic except on $\partial\Omega$, one straightforward approach is to penalize its (discrete) Laplacian
 131 on points $\mathbf{x} \notin \partial\Omega$. However, it is in general difficult to explicitly model this harmonic incom-
 132 patibility and/or to directly impose its property into the susceptibility reconstruction model
 133 due to the complicated geometries of human brains and the limited spatial resolution in real
 134 MRI data. Instead, we impose the sparse regularization of the incompatibility as the support
 135 of its Laplacian is small compared to the size of image. Combing it with traditional regular-
 136 ization on the susceptibility image, we propose a novel regularization based QSM model by
 137 imposing additional constraints on the incompatibility term. Within the new model, we can
 138 suppress the incompatibility other than the noise, achieving the whole brain imaging with less
 139 artifacts together with the regularization of susceptibility image. Experiments on both brain
 140 phantom and vivo MR data consistently show the advantages of the proposed HIRE model
 141 which achieves the state-of-the-art performance. Besides, our experiments suggest that tight
 142 frame regularization of the susceptibility image can avoid the constant offset [27] and lead to
 143 efficient computation.

144 **1.3. Organization of Paper.** In section 2, we introduce our HIRE model for whole brain
 145 susceptibility imaging. More precisely, we first briefly review the biophysics forward model of
 146 QSM in subsection 2.1, and characterize the harmonic incompatibility in the local field data
 147 in subsection 2.2. Based on the characterization, we introduce the proposed HIRE model
 148 in subsection 2.3, followed by an alternating minimization algorithm in subsection 2.4. In
 149 section 3, we present experimental results for both brain phantom and in vivo MR data, and
 150 the concluding remarks are given in section 4.

151 2. Harmonic Incompatibility Removal (HIRE) Model for Whole Brain Imaging.

152 **2.1. Preliminaries on Biophysics of QSM.** In an MRI scanner with the main static mag-
 153 netic field $\mathbf{B}_0 = (0, 0, B_0)$ where B_0 is a positive constant, objects gain a magnetization $\mathbf{M}(\mathbf{x})$.
 154 This magnetization generates a macroscopic field $\mathbf{B}(\mathbf{x})$ satisfying the following magnetostatic
 155 Maxwell's equation [23, 45]

$$\begin{aligned} 156 \quad & \nabla \cdot \mathbf{B} = 0 \\ 157 \quad & \nabla \times \mathbf{B} = \mu_0 \nabla \times \mathbf{M}, \end{aligned} \tag{2.1}$$

158 where $\mu_0 = 8.854 \times 10^{-12}$ F/m is the vacuum permittivity. Since the MRI signal is generated
 159 by the microscopic field $\mathbf{B}_\ell(\mathbf{x})$ experienced by the spins of water protons [27], we use the
 160 following Lorenz sphere correction model [23]:

$$161 \quad \mathbf{B}_\ell(\mathbf{x}) = \mathbf{B}(\mathbf{x}) - \frac{2}{3}\mu_0\mathbf{M}(\mathbf{x}) \tag{2.2}$$

162 to relate $\mathbf{B}(\mathbf{x})$ and $\mathbf{B}_\ell(\mathbf{x})$.

163 Note that since $\mathbf{M}(\mathbf{x})$ is generated by \mathbf{B}_0 field, we have $\mathbf{M}(\mathbf{x}) = (0, 0, M(\mathbf{x}))$. Moreover,
 164 since we consider the linear magnetic materials with $|\chi| \ll 1$, χ can be approximated as

$$166 \quad \chi(\mathbf{x}) \approx \frac{\mu_0}{B_0}\mathbf{M}(\mathbf{x}). \tag{2.3}$$

167 Finally, we introduce the total field $b(\mathbf{x})$ as

$$169 \quad b(\mathbf{x}) = \frac{B_{\ell 3}(\mathbf{x}) - B_0}{B_0} \tag{2.4}$$

170 where $B_{\ell 3}(\mathbf{x})$ denotes the third component of $\mathbf{B}_\ell(\mathbf{x})$.

171 Combining (2.1)–(2.4) and taking the third component into account only, we obtain the
 172 following relation between χ and b in the frequency domain:

$$174 \quad |\boldsymbol{\xi}|^2 \mathcal{F}(b)(\boldsymbol{\xi}) = \left(\frac{1}{3}|\boldsymbol{\xi}|^2 - \xi_3^2 \right) \mathcal{F}(\chi)(\boldsymbol{\xi}), \tag{2.5}$$

175 which gives

$$177 \quad -\Delta b = P(D)\chi := \left(-\frac{1}{3}\Delta + \frac{\partial^2}{\partial x_3^2} \right) \chi. \tag{2.6}$$

178

179 Then for a given susceptibility distribution χ (in \mathbb{R}^3), the general solution b which is bounded
 180 everywhere in \mathbb{R}^3 is expressed as

$$181 \quad b(\mathbf{x}) = \int_{\mathbb{R}^3} \Phi(\mathbf{x} - \mathbf{y}) \left(-\frac{1}{3} \Delta_{\mathbf{y}} + \frac{\partial^2}{\partial y_3^2} \right) \chi(\mathbf{y}) d\mathbf{y} + b_0 \quad (2.7)$$

183 where b_0 is some constant, and $\Phi(\mathbf{x}) = 1/(4\pi|\mathbf{x}|)$.

184 In MRI, the phase of a complex GRE MR signal is linear with respect to the total field
 185 b in (2.7) [52], and the constant b_0 is determined by the coil sensitivity of an MR scanner
 186 as the coil sensitivity dependent phase offset is in general assumed to be a constant [24, 44].
 187 However, since we can remove it during the phase estimation from the multi echo GRE signal
 188 [12], we assume that $b_0 = 0$ and

$$189 \quad b(\mathbf{x}) = \int_{\mathbb{R}^3} \Phi(\mathbf{x} - \mathbf{y}) \left(-\frac{1}{3} \Delta_{\mathbf{y}} + \frac{\partial^2}{\partial y_3^2} \right) \chi(\mathbf{y}) d\mathbf{y} \quad (2.8)$$

191 in the rest of this paper. Note that b defined as above is induced by the susceptibility distri-
 192 bution *in the entire space*, which is different from b_l in (1.3).

193 **Remark 2.1.** *Since [9, Proposition A.1.] has discussed the equivalence between (2.8) and*
 194 *the following representation in the literature*

$$195 \quad b(\mathbf{x}) = \text{pv} \int_{\mathbb{R}^3} d(\mathbf{x} - \mathbf{y}) \chi(\mathbf{y}) d\mathbf{y}, \quad (2.9)$$

197 *we shall use (2.8) in the rest of this paper. Note that (2.8) avoids the singularity of the kernel*
 198 *$d(\mathbf{x} - \mathbf{y})$ in (2.9) as $\Phi(\mathbf{x} - \mathbf{y})$ is locally integrable near $\mathbf{x} = \mathbf{y}$.*

199 **2.2. Characterization of Harmonic Incompatibility in Local Field Data.** In QSM, the
 200 total field $b(\mathbf{x})$ is obtained from the phase data of a complex GRE MR signal [44, 52]. In fact,
 201 if the information of b is available over the entire space, then we can directly solve inverse
 202 problem from the knowledge of b without the background field removal step. However, since
 203 the GRE signal is not available outside Ω , the information of b is available only inside Ω .
 204 Moreover, even if χ is compactly supported, the support of b may not necessarily coincide
 205 with that of χ , which inevitably leads to the information loss outside Ω [44, 52].

206 Since the total field b depends on the susceptibility distribution *throughout the entire space*
 207 [44], it consists of the background field induced from the susceptibility outside Ω , which is of
 208 no interest, and the local field b_l by the susceptibility in Ω which we aim to visualize. Since the
 209 substantial susceptibility sources are usually located outside Ω which makes the background
 210 field dominant in b compared to the local field b_l , we need to remove the background field
 211 from the (incomplete) total field prior to the dipole inversion [44, 52].

212 In the literature, given that the background field is harmonic in Ω [52, 57], the background
 213 field removal methods take the form of the following Poisson's equation in [57]:

$$214 \quad \begin{cases} -\Delta b_l = -\Delta b & \text{in } \Omega \\ b_l = 0 & \text{on } \partial\Omega. \end{cases} \quad (2.10)$$

215

216 Under this setting, we present [Theorem 2.2](#) which characterizes the relation between [\(2.10\)](#)
 217 and the PDE [\(2.6\)](#), and the measured local field obtained by solving [\(2.10\)](#) contains an in-
 218 compatibility which consists of two harmonic functions both inside and outside Ω due to the
 219 imposed boundary condition.

220 [Theorem 2.2.](#) Let $\Omega \subseteq \mathbb{R}^3$ be an open and bounded set with C^1 boundary $\partial\Omega$. Let b satisfy
 221 [\(2.8\)](#) for a given χ compactly supported in \mathbb{R}^3 , and let $b_l : \bar{\Omega} \rightarrow \mathbb{R}$ be obtained from [\(2.10\)](#). If
 222 we extend b_l into \mathbb{R}^3 by assigning $b_l(\mathbf{x}) = 0$ for $\mathbf{x} \notin \Omega$, then we have the followings:

223 1. There exists $v(x)$ such that

$$224 \quad b_l(\mathbf{x}) = \int_{\Omega} \Phi(\mathbf{x} - \mathbf{y}) \left(-\frac{1}{3} \Delta_{\mathbf{y}} + \frac{\partial^2}{\partial y_3^2} \right) \chi(\mathbf{y}) d\mathbf{y} + v(\mathbf{x}) \quad (2.11)$$

225
 226 for $\mathbf{x} \in \mathbb{R}^3$, and $v(\mathbf{x})$ satisfies

$$227 \quad \int_{\mathbb{R}^3} v(\mathbf{x}) (-\Delta\varphi)(\mathbf{x}) d\mathbf{x} = \int_{\partial\Omega} \left[\frac{\partial v_i}{\partial \mathbf{n}}(\mathbf{x}) - \frac{\partial v_e}{\partial \mathbf{n}}(\mathbf{x}) \right] \varphi(\mathbf{x}) d\boldsymbol{\sigma}(\mathbf{x}) \quad (2.12)$$

228
 229 for $\varphi \in C_0^\infty(\mathbb{R}^3)$, where v_i and v_e denote the restriction of v in $\bar{\Omega}$ and $\mathbb{R}^3 \setminus \Omega$ respectively,
 230 and \mathbf{n} denotes the outward unit normal vector of $\partial\Omega$.

231 2. Moreover, we have

$$232 \quad \frac{\partial v_i}{\partial \mathbf{n}} - \frac{\partial v_e}{\partial \mathbf{n}} \neq 0 \quad \text{almost everywhere on } \partial\Omega \quad (2.13)$$

233
 234 whenever $P(D)\chi \neq 0$ in Ω . Hence, $-\Delta v = 0$ in $\mathbb{R}^3 \setminus \partial\Omega$, and $-\Delta v \neq 0$ on $\partial\Omega$ in this
 235 case.

236 *Proof.* Since $-\Delta b = P(D)\chi$, the governing equation in [\(2.10\)](#) becomes

$$237 \quad \begin{cases} -\Delta b_l = P(D)\chi & \text{in } \Omega \\ b_l = 0 & \text{on } \partial\Omega. \end{cases}$$

238
 239 Let $G(\mathbf{x}, \mathbf{y})$ denote the Green's function in Ω :

$$240 \quad G(\mathbf{x}, \mathbf{y}) = \Phi(\mathbf{y} - \mathbf{x}) - H(\mathbf{x}, \mathbf{y})$$

241
 242 where for each $\mathbf{x} \in \Omega$, the corrector function $H(\mathbf{x}, \mathbf{y})$ satisfies

$$243 \quad \begin{cases} -\Delta_{\mathbf{y}} H(\mathbf{x}, \mathbf{y}) = 0 & \text{if } \mathbf{y} \in \Omega \\ H(\mathbf{x}, \mathbf{y}) = \Phi(\mathbf{y} - \mathbf{x}) & \text{if } \mathbf{y} \in \partial\Omega. \end{cases}$$

244
 245 Note that since $G(\mathbf{x}, \mathbf{y}) = G(\mathbf{y}, \mathbf{x})$ for $\mathbf{x}, \mathbf{y} \in \Omega$ and $\Phi(\mathbf{y} - \mathbf{x}) = \Phi(\mathbf{x} - \mathbf{y})$, we have $H(\mathbf{x}, \mathbf{y}) =$
 246 $H(\mathbf{y}, \mathbf{x})$ for $\mathbf{x}, \mathbf{y} \in \Omega$. Consequently, we have

$$247 \quad -\Delta_{\mathbf{x}} H(\mathbf{x}, \mathbf{y}) = -\Delta_{\mathbf{x}} H(\mathbf{y}, \mathbf{x}) = 0 \quad \mathbf{x} \in \Omega. \quad (2.14)$$

248
 249 Then the solution to [\(2.10\)](#) is represented as

$$250 \quad b_l(\mathbf{x}) = \int_{\Omega} G(\mathbf{x}, \mathbf{y}) P(D_{\mathbf{y}}) \chi(\mathbf{y}) d\mathbf{y} = \int_{\Omega} \Phi(\mathbf{x} - \mathbf{y}) P(D_{\mathbf{y}}) \chi(\mathbf{y}) d\mathbf{y} + \mathcal{H}(\mathbf{x})$$

251

252 where we used the fact that $\Phi(\mathbf{y} - \mathbf{x}) = \Phi(\mathbf{x} - \mathbf{y})$, and $\mathcal{H}(\mathbf{x})$ is defined as

$$253 \quad \mathcal{H}(\mathbf{x}) = - \int_{\Omega} H(\mathbf{x}, \mathbf{y}) P(D_{\mathbf{y}}) \chi(\mathbf{y}) d\mathbf{y}$$

254 for $\mathbf{x} \in \Omega$. Then we can see that $\mathcal{H}(\mathbf{x})$ satisfies

$$256 \quad \begin{cases} -\Delta \mathcal{H} = 0 & \text{in } \Omega \\ \mathcal{H} = -\tilde{b}_l & \text{on } \partial\Omega \end{cases} \quad (2.15)$$

257 where the first equation of (2.15) comes from (2.14). Here, \tilde{b}_l is induced by the information
258 of χ only in Ω :

$$260 \quad \tilde{b}_l(\mathbf{x}) = \int_{\Omega} \Phi(\mathbf{x} - \mathbf{y}) P(D_{\mathbf{y}}) \chi(\mathbf{y}) d\mathbf{y} = \int_{\mathbb{R}^3} \Phi(\mathbf{x} - \mathbf{y}) 1_{\Omega}(\mathbf{y}) P(D_{\mathbf{y}}) \chi(\mathbf{y}) d\mathbf{y} \quad (2.16)$$

261 with 1_{Ω} being the characteristic function of Ω .

262 Based on the fact that $b_l(\mathbf{x}) = 0$ for $\mathbf{x} \in \mathbb{R}^3 \setminus \bar{\Omega}$, we define

$$264 \quad v(\mathbf{x}) = \begin{cases} v_i(\mathbf{x}) = \mathcal{H}(\mathbf{x}) & \text{if } \mathbf{x} \in \Omega \\ v_e(\mathbf{x}) = -\tilde{b}_l(\mathbf{x}) & \text{if } \mathbf{x} \notin \Omega. \end{cases}$$

265 Hence, we obtain (2.11), and we can further see that v_i and v_e satisfy

$$267 \quad -\Delta v_i = 0 \quad \text{in } \Omega \quad (2.17)$$

$$268 \quad -\Delta v_e = 0 \quad \text{in } \mathbb{R}^3 \setminus \bar{\Omega} \quad (2.18)$$

$$269 \quad v_i = v_e = -\tilde{b}_l \quad \text{on } \partial\Omega, \quad (2.19)$$

271 respectively, where (2.18) comes from (2.16); $-\Delta \tilde{b}_l = 1_{\Omega} P(D) \chi$, i.e. $-\Delta \tilde{b}_l = P(D) \chi$ in Ω ,
272 and $-\Delta \tilde{b}_l = 0$ in $\mathbb{R}^3 \setminus \bar{\Omega}$.

273 To prove (2.12), let $\varphi \in C_0^{\infty}(\mathbb{R}^3)$, and we consider

$$274 \quad \int_{\mathbb{R}^3} v(\mathbf{x}) (-\Delta \varphi)(\mathbf{x}) d\mathbf{x} = \int_{\Omega} v_i(\mathbf{x}) (-\Delta \varphi)(\mathbf{x}) d\mathbf{x} + \int_{\mathbb{R}^3 \setminus \bar{\Omega}} v_e(\mathbf{x}) (-\Delta \varphi)(\mathbf{x}) d\mathbf{x}$$

$$275 \quad = I_1 + I_2$$

276 Using (2.17) and (2.19) and the Green's identity (e.g. [19]), we have

$$278 \quad I_1 = \int_{\Omega} [\varphi(\mathbf{x}) (\Delta v_i)(\mathbf{x}) - v_i(\mathbf{x}) (\Delta \varphi)(\mathbf{x})] d\mathbf{x}$$

$$279 \quad = \int_{\partial\Omega} \left[\varphi(\mathbf{x}) \frac{\partial v_i}{\partial \mathbf{n}}(\mathbf{x}) - v_i(\mathbf{x}) \frac{\partial \varphi}{\partial \mathbf{n}}(\mathbf{x}) \right] d\boldsymbol{\sigma}(\mathbf{x}) = \int_{\partial\Omega} \left[\varphi(\mathbf{x}) \frac{\partial v_i}{\partial \mathbf{n}}(\mathbf{x}) + \tilde{b}_l(\mathbf{x}) \frac{\partial \varphi}{\partial \mathbf{n}}(\mathbf{x}) \right] d\boldsymbol{\sigma}(\mathbf{x}).$$

280 Similarly using (2.18) and (2.19), we also have

$$282 \quad I_2 = \int_{\mathbb{R}^3 \setminus \bar{\Omega}} [\varphi(\mathbf{x}) (\Delta v_e)(\mathbf{x}) - v_e(\mathbf{x}) (\Delta \varphi)(\mathbf{x})] d\mathbf{x}$$

$$283 \quad = \int_{\partial\Omega} \left[-\varphi(\mathbf{x}) \frac{\partial v_e}{\partial \mathbf{n}}(\mathbf{x}) + v_e(\mathbf{x}) \frac{\partial \varphi}{\partial \mathbf{n}}(\mathbf{x}) \right] d\boldsymbol{\sigma}(\mathbf{x}) = - \int_{\partial\Omega} \left[\varphi(\mathbf{x}) \frac{\partial v_e}{\partial \mathbf{n}}(\mathbf{x}) + \tilde{b}_l(\mathbf{x}) \frac{\partial \varphi}{\partial \mathbf{n}}(\mathbf{x}) \right] d\boldsymbol{\sigma}(\mathbf{x})$$

285 where the second equality comes from the fact that we need to compute the inward normal
 286 derivatives on $\partial\Omega$. Hence, combining these two equalities, we obtain (2.12).

287 To prove 2, we assume on the contrary that there exists $\mathbf{x} \in \partial\Omega$ such that

$$288 \quad \frac{\partial v_i}{\partial \mathbf{n}} = \frac{\partial v_e}{\partial \mathbf{n}}$$

289
 290 for some open and connected set $U \subseteq \partial\Omega$ such that $\mathbf{x} \in U$ and $\sigma(U) > 0$. Choose $r > 0$ such
 291 that $B(\mathbf{x}, r) \cap \partial\Omega$ is contained in U , where $B(\mathbf{x}, r)$ denotes an open ball centered at \mathbf{x} with
 292 radius r . Then since $-\Delta v = 0$ in $B(\mathbf{x}, r)$ and $v = v_e = -\tilde{b}_l$ in $B(\mathbf{x}, r) \cap (\mathbb{R}^3 \setminus \bar{\Omega})$, it follows
 293 that $v = -\tilde{b}_l$ in $B(\mathbf{x}, r)$ by the analyticity of v in $B(\mathbf{x}, r)$. Since this means that $v = v_i = -\tilde{b}_l$
 294 in $B(\mathbf{x}, r) \cap \Omega$, together with the fact that v_i is harmonic in Ω , we have $v_i = -\tilde{b}_l$ in Ω by the
 295 analyticity of v_i in Ω . Since $v = -\tilde{b}_l$ on $\partial\Omega$, we have $v = -\tilde{b}_l$ in \mathbb{R}^3 . Hence, $-\Delta \tilde{b}_l = 0$ in \mathbb{R}^3 ,
 296 and thus, $P(D)\chi = 0$ in Ω , which is a contradiction. ■

297 **Remark 2.3.** From the proof of [Theorem 2.2](#), the incompatibility v in (2.11) is from the
 298 boundary condition of (2.10) which is not related to the regularity of χ . More precisely, v_i
 299 inside Ω is generated by the information of the unknown true local field b_l on $\partial\Omega$ so that the
 300 boundary condition of (2.10) is matched. In addition, it is obvious that v_e outside Ω is due to
 301 the information loss outside Ω .

302 **Remark 2.4.** Notice that $P(D)$ is a “wave type” differential operator (by considering x_3 as
 303 the time variable). Indeed, the proof of (2.13) tells us that if $P(D)\chi = 0$ in Ω , such χ has a
 304 wave type structure in Ω regardless of its regularity, whereas the susceptibility of human brain
 305 does not have such a wave type structure [9]. Hence in QSM, it follows that $-\Delta v$ defined as
 306 (2.12) is a nonvanishing surface measure on $\partial\Omega$, i.e. $-\Delta v = 0$ in $\mathbb{R}^3 \setminus \partial\Omega$, but $-\Delta v \neq 0$ on
 307 $\partial\Omega$.

308 We present [Figures 2](#) to [5](#) to illustrate [Theorem 2.2](#) by using the Shepp-Logan phantom
 309 ([Figures 2](#) and [3](#)) and the brain phantom ([Figures 4](#) and [5](#)). Using the limited total field b in
 310 [Figures 2d, 3d, 4d](#) and [5d](#) which are derived from (2.8) by placing strong susceptibilities outside
 311 Ω , we solve (2.10) using multigrid (MG) based the finite difference method [57] to obtain the
 312 measured local field b_l in [Figures 2f, 3f, 4f](#) and [5f](#) which are used for the susceptibility
 313 reconstruction. We also display the true local field \tilde{b}_l obtained from (2.16) in [Figures 2e,](#)
 314 [3e, 4e](#) and [5e](#) for the comparison with the measured b_l . Finally, $v = b_l - \tilde{b}_l$ and $|\Delta v|$
 315 are displayed in [Figures 2g, 3g, 4g](#) and [5g](#) and [Figures 2h, 3h, 4h](#) and [5h](#) respectively for
 316 better illustrations. Compared to the Shepp-Logan phantom, the brain phantom shows the
 317 artifacts as shown in [Figure 4h](#). There are two possible reasons of the artifacts. Firstly,
 318 since the boundary of human brain is more complicated than the Shepp-Logan phantom, the
 319 erroneous boundary values may have affected the background field removal in the case of brain
 320 phantom, as pointed out in [57]. Secondly, unlike the Shepp-Logan phantom with isotropic
 321 spatial resolution ($1 \times 1 \times 1\text{mm}^3$), the brain phantom has an anisotropic spatial resolution
 322 of $0.9375 \times 0.9375 \times 1.5\text{mm}^3$. As pointed out in [20], the MG method has a limitation that
 323 errors in certain directions (x_3 direction in our case) are not smoothed by standard relaxation
 324 and as a consequence, it is inappropriate to coarsen in these directions, which may lead to
 325 artifacts in [Figure 4h](#) along the x_3 direction. Since the real spatial resolution of phase data
 326 is not necessarily isotropic, an efficient and effective numerical solver of (2.10) need to be
 327 investigated in the future, which is beyond the scope of this paper at this point.

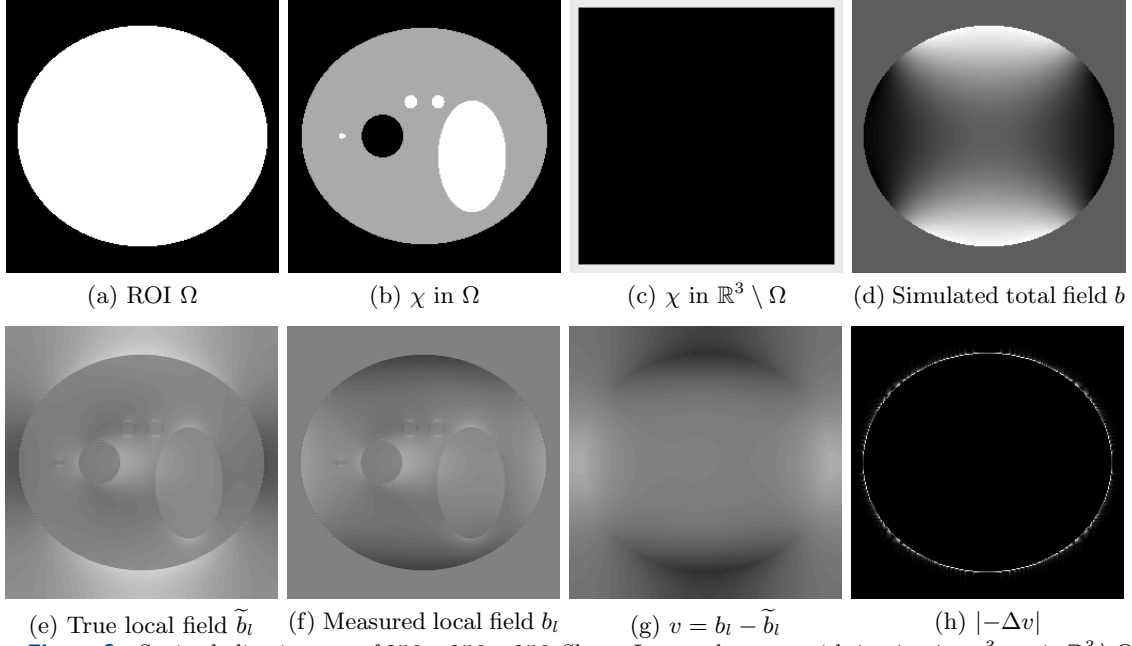


Figure 2. Sagittal slice images of $256 \times 256 \times 256$ Shepp-Logan phantom with $1 \times 1 \times 1 \text{mm}^3$. χ in $\mathbb{R}^3 \setminus \Omega$ is displayed in the window level $[0, 550]$, \tilde{b}_l , b_l and v in the window level $[-0.025, 0.025]$, and $|\Delta v|$ in the window level $[0, 0.001]$.

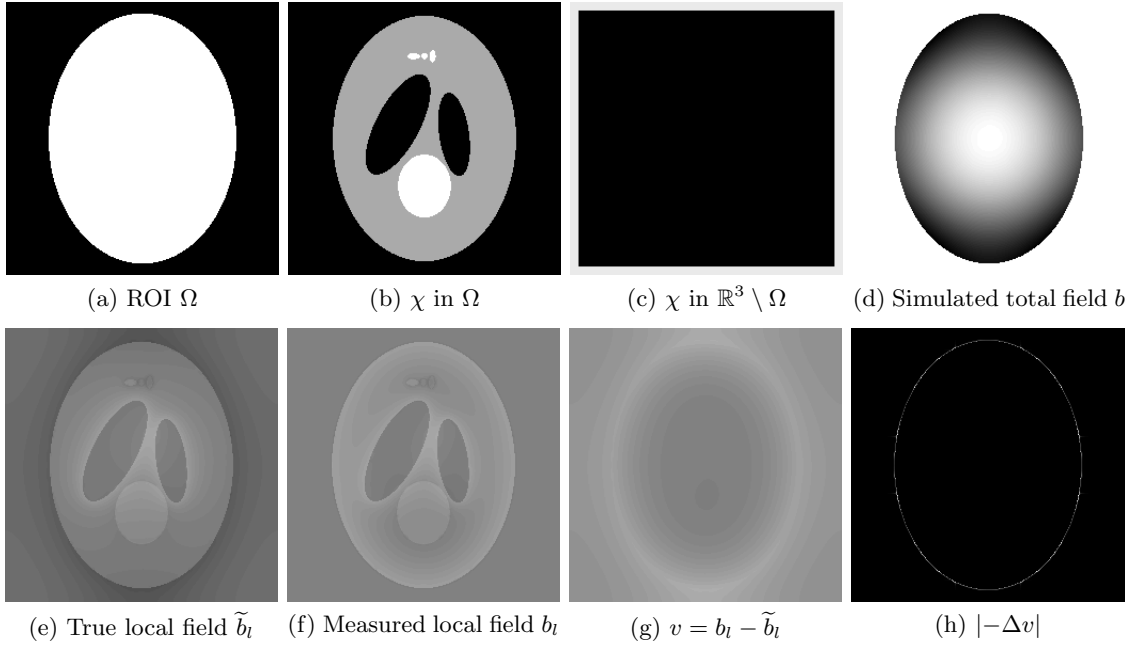


Figure 3. Axial slice images of Figure 2. The images of χ in $\mathbb{R}^3 \setminus \Omega$, \tilde{b}_l , b_l , v , and $|\Delta v|$ are displayed in the same window level as Figure 2.

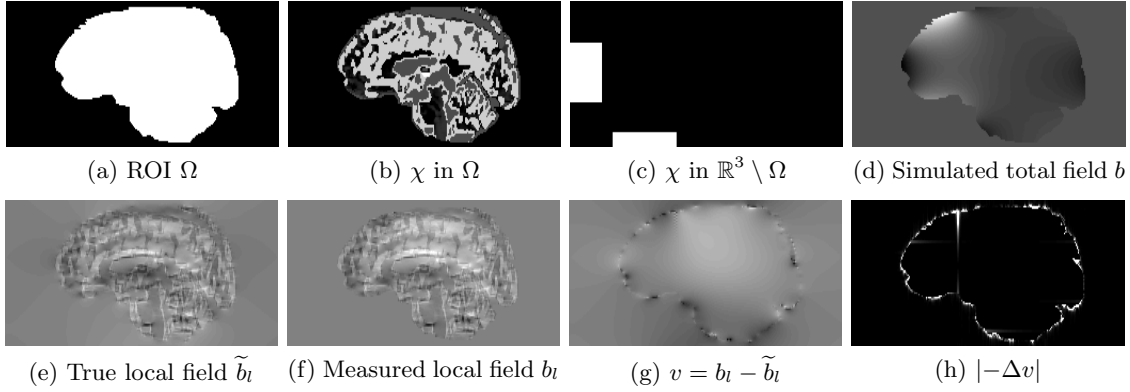


Figure 4. Sagittal slice images of $256 \times 256 \times 98$ brain phantom images with $0.9375 \times 0.9375 \times 1.5\text{mm}^3$. Image of χ in $\mathbb{R}^3 \setminus \Omega$ is displayed in the window level $[0, 500]$, \tilde{b}_l and b_l in the window level $[-0.05, 0.05]$, v in the window level $[-0.025, 0.025]$, and $|\Delta v|$ in the window level $[0, 0.01]$ respectively.

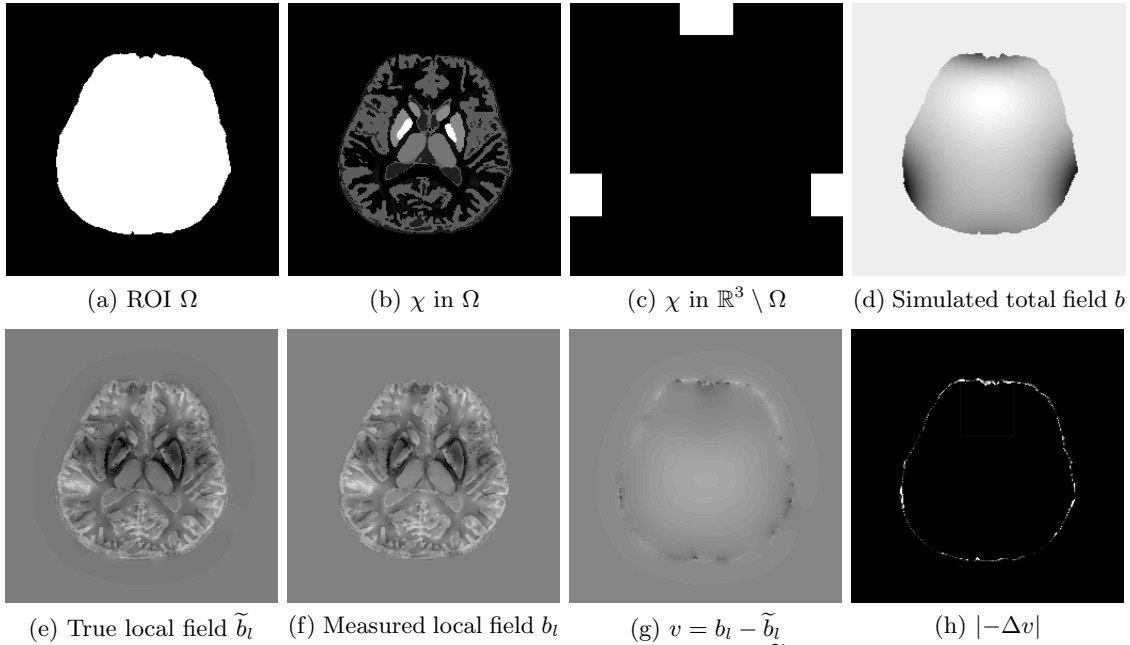


Figure 5. Axial slice images of [Figure 4](#). The images of χ in $\mathbb{R}^3 \setminus \Omega$, \tilde{b}_l , b_l , v , and $|\Delta v|$ are displayed in the same window level as [Figure 4](#).

328 **2.3. Proposed HIRE Susceptibility Reconstruction Model.** We begin with introducing
 329 some notation. Let $\mathbb{O} = \{0, \dots, N_1 - 1\} \times \{0, \dots, N_2 - 1\} \times \{0, \dots, N_3 - 1\}$ denote the set
 330 of indices of $N_1 \times N_2 \times N_3$ grids, and let $\Omega \subseteq \mathbb{O}$ denote the set of indices corresponding to the
 331 ROI. Denote $\partial\Omega$ to be the indices of the boundary of ROI Ω . Finally, the space of real valued
 332 functions defined on \mathbb{O} is denoted as $\mathcal{I}_3 \simeq \mathbb{R}^{N_1 \times N_2 \times N_3}$.

333 Let $b_l \in \mathcal{I}_3$ be the (noisy) measured local field data obtained from [\(2.10\)](#), which satisfies

334 $b_l = 0$ in $\mathbb{O} \setminus \Omega$. From the viewpoint of [Theorem 2.2](#), we can model it as

$$335 \quad b_l = A\chi + v + \eta$$

337 where $A = \mathcal{F}^{-1}\mathcal{D}\mathcal{F}$ denotes the discretization of the forward operator in [\(2.11\)](#). Here, $\chi \in \mathcal{I}_3$
338 is the unknown true susceptibility image supported in Ω , $v \in \mathcal{I}_3$ is the incompatibility arising
339 from solving [\(2.10\)](#), and η is the additive noise.

340 We observe that in the discrete setting, [\(2.12\)](#) in [Theorem 2.2](#) can be understood as

$$341 \quad \mathcal{L}v = 0 \quad \text{in } \mathbb{O} \setminus \partial\Omega \quad \text{and} \quad \mathcal{L}v \neq 0 \quad \text{on } \partial\Omega \quad (2.20)$$

343 with the discrete Laplacian \mathcal{L} , as $\mathcal{L}v$ is supported on $\partial\Omega$. However, it is in general dif-
344 ficult to directly impose [\(2.20\)](#) into the susceptibility reconstruction model (e.g. penalizing
345 $\|(\mathcal{L}v)_{\mathbb{O} \setminus \partial\Omega}\|_2^2$) for the following reasons: 1) the estimation of Ω always contains error due to the
346 complicated geometry of the human brain; 2) the real MRI data may not exactly satisfy [\(2.20\)](#)
347 due to its spatial resolution [\[23\]](#); 3) the discretization can introduce the error on the boundary
348 of Ω . However, it is a fact that the support of $\mathcal{L}v$ is small compared to $|\mathbb{O}| = N_1N_2N_3$, i.e. $\mathcal{L}v$
349 is sparse. Consequently, we penalize the $\|\mathcal{L}v\|_1$ for the incompatibility term v . Although the
350 $\|\mathcal{L}v\|_1$ does not necessarily satisfy the harmonic constraints on $\mathbb{O} \setminus \partial\Omega$, it is a good relaxation
351 approach when considering the error source of the forward model in QSM. In addition, moti-
352 vated by the successful results on the wavelet frame based image restoration (e.g. [\[3, 4\]](#)), we
353 assume the sparse approximation of χ under a given wavelet transformation W , and propose
354 our HIRE model as follows:

$$355 \quad \min_{\chi, v \in \mathcal{I}_3} \frac{1}{2} \|A\chi + v - b_l\|_{\Sigma}^2 + \lambda \|\mathcal{L}v\|_1 + \|\gamma \cdot W\chi\|_{1,2} \quad (2.21)$$

357 where $\|\cdot\|_{\Sigma}^2 = \langle \Sigma \cdot, \cdot \rangle$ with the SNR weight Σ which is estimated from the MRI [\[32, 38\]](#). Here,
358 $\|\gamma \cdot W\chi\|_{1,2}$ is the isotropic ℓ_1 norm of the wavelet frame coefficients [\[4\]](#) defined as

$$359 \quad \|\gamma \cdot W\chi\|_{1,2} := \sum_{\mathbf{k} \in \mathbb{O}} \sum_{l=0}^{L-1} \gamma_l[\mathbf{k}] \left(\sum_{\alpha \in \mathbb{B}} |(W_{l,\alpha}\chi)[\mathbf{k}]|^2 \right)^{1/2}. \quad (2.22)$$

361 (See [Appendix A](#) for the brief introduction on the wavelet frames.)

362 There are many variational regularizations for the susceptibility image including total
363 variation (TV) [\[42\]](#), total generalized variation (TGV) [\[2, 55\]](#), and weighted TV for morpho-
364 logical consistency [\[26\]](#). However, since $\mathcal{D}(\mathbf{0}) = 0$, the χ subproblem is a rank deficient system
365 matrix, when using the alternating direction method of multipliers (ADMM) methods [\[18\]](#)
366 to solve the regularization model. As a consequence, we may need additional prior informa-
367 tion such as the zero susceptibility value in the cerebrospinal fluid region [\[36\]](#) for the stable
368 reconstruction. In contrast, by using the tight frame regularization, the system matrix of χ
369 subproblem has a full column rank, which can lead to the computational efficiency over the
370 existing variational methods.

371 **Remark 2.5.** For better understanding of our HIRE model, we temporarily assume that
372 $\Sigma = I$ and consider

$$373 \quad \min_{\chi, v \in \mathcal{I}_3} \frac{1}{2} \|A\chi + v - b_l\|_2^2 + \lambda \|\mathcal{L}v\|_1 + \|\gamma \cdot W\chi\|_{1,2}.$$

374

375 If $v \equiv 0$, our model reduces to the integral approach model:

$$376 \quad \min_{\chi \in \mathcal{I}_3} \frac{1}{2} \|A\chi - b_l\|_2^2 + \|\gamma \cdot W\chi\|_{1,2}.$$

377

378 In addition, if we fix $v = b_l - A\chi$, our model reduces to the ℓ_1 fidelity version of the following
379 differential approach model:

$$380 \quad \min_{\chi \in \mathcal{I}_3} \frac{1}{2} \|\mathcal{L}b_l - \mathcal{L}A\chi\|_2^2 + \|\gamma \cdot W\chi\|_{1,2}$$

381

382 as $\mathcal{L}A\chi = \mathcal{L}b_l$ discretizes the PDE (2.6) in the sense of [9, Proposition A.1.].

383 From Remark 2.5, we can see that our model considers the incompatibility v and noise
384 separately, thereby providing a more precise forward model for QSM. This is because b_l is
385 obtained from the Poisson's equation (2.10) and it inevitably contains the harmonic incompat-
386 ibility related to the imposed boundary condition, as described in Theorem 2.2. Even though
387 more rigorous theoretical analysis is needed, we can somehow explain the effect of harmonic
388 incompatibility in this manner; since the standard arguments on the harmonic functions (e.g.
389 [19]) tell us that v is smooth and satisfies the mean value property except on $\partial\Omega$, it has slow
390 variations on this region. As a consequence, it mostly affects the low frequency components in
391 b_l compared to the noise which mainly affects the high frequency components. Together with
392 the fact that the critical manifold Γ_0 forms a conic manifold in the frequency domain, the
393 harmonic incompatibility v in b_l mainly leads to the loss of $\mathcal{F}(\chi)$ in low frequency components.

394 As empirically observed in [27], the incompatibility in low frequency components of b_l
395 leads to the shadow artifacts in the reconstructed image, while that in high frequency com-
396 ponents leads to the streaking artifacts. Therefore, the simultaneous consideration on the
397 incompatibilities in both components is crucial for better susceptibility imaging. The integral
398 approach does not take the harmonic incompatibility in b_l into account, which may not be
399 capable of suppressing the incompatibility in low frequency components of b_l , and leads to
400 the shadow artifacts in the reconstructed images. The differential approach can be viewed
401 as a preconditioned integral approach since the harmonic incompatibility in b_l has been re-
402 moved in advance. However, the noise in b_l can be amplified by \mathcal{L} at the cost of harmonic
403 incompatibility removal, and this leads to the streaking artifacts propagating from the noise
404 in final image [52]. In contrast, the HIRE model takes the form of integral approach which
405 explicitly considers the incompatibility v other than the noise by incorporating its sparsity
406 under \mathcal{L} . By doing so, we expect that the HIRE model can suppress both the noise (cause of
407 streaking artifacts) and the harmonic incompatibility (cause of shadow artifacts), so that we
408 can achieve the whole brain imaging with less artifacts.

409 We would like to mention that the formulation of HIRE model is not limited to (2.21). In
410 fact, we can use the nonlinear fidelity term $F(b_l|\chi, v) = \frac{1}{2} \|e^{i(A\chi+v)\omega_0 B_0 TE} - e^{ib_l\omega_0 B_0 TE}\|_{\Sigma}^2$ to
411 further compensate the errors in phase unwrapping, which will be more coincident with the
412 GRE signal model [27, 35]. However, we will not discuss the details on such nonlinear variants
413 as this is beyond the scope of this paper. We will focus on (2.21) throughout this paper.

414 **2.4. Numerical Algorithm.** In the literature, there are numerous algorithms which can
415 solve the proposed HIRE model (2.21). In this paper, we adopt the split Bregman algorithm

Algorithm 1 Split Bregman Algorithm for (2.21)**Initialization:** $\chi^0, v^0, d^0, e^0, f^0, g^0, p^0, q^0, r^0, s^0$ **for** $k = 0, 1, 2, \dots$ **do** Update χ and v :

$$\chi^{k+1} = \underset{\chi}{\operatorname{argmin}} \frac{\beta}{2} \|A\chi - f^k + r^k\|_2^2 + \frac{\beta}{2} \|W\chi - d^k + p^k\|_2^2 \quad (2.23)$$

$$v^{k+1} = \underset{v}{\operatorname{argmin}} \frac{\beta}{2} \|v - g^k + s^k\|_2^2 + \frac{\beta}{2} \|\mathcal{L}v - e^k + q^k\|_2^2 \quad (2.24)$$

 Update d, e, f , and g :

$$d^{k+1} = \underset{d}{\operatorname{argmin}} \|\gamma \cdot d\|_{1,2} + \frac{\beta}{2} \|d - W\chi^{k+1} - p^k\|_2^2 \quad (2.25)$$

$$e^{k+1} = \underset{e}{\operatorname{argmin}} \lambda \|e\|_1 + \frac{\beta}{2} \|e - \mathcal{L}v^{k+1} - q^k\|_2^2 \quad (2.26)$$

$$f^{k+1} = \underset{f}{\operatorname{argmin}} \frac{1}{2} \|f + g^k - b_l\|_\Sigma^2 + \frac{\beta}{2} \|f - A\chi^{k+1} - r^k\|_2^2 \quad (2.27)$$

$$g^{k+1} = \underset{g}{\operatorname{argmin}} \frac{1}{2} \|g + f^{k+1} - b_l\|_\Sigma^2 + \frac{\beta}{2} \|g - v^{k+1} - s^k\|_2^2 \quad (2.28)$$

 Update p, q, r , and s :

$$p^{k+1} = p^k + W\chi^{k+1} - d^{k+1} \quad (2.29)$$

$$q^{k+1} = q^k + \mathcal{L}v^{k+1} - e^{k+1} \quad (2.30)$$

$$r^{k+1} = r^k + A\chi^{k+1} - f^{k+1} \quad (2.31)$$

$$s^{k+1} = s^k + v^{k+1} - g^{k+1} \quad (2.32)$$

end for

416 given in [38] in the framework of ADMM [18] as we can convert (2.21) into several subproblems
 417 which can be solved efficiently. More precisely, let $d = W\chi$, $e = \mathcal{L}v$, $f = A\chi$, and $g = v$.
 418 Then (2.21) is reformulated as follows:

$$419 \quad \min_{\chi, v, d, e, f, g} \frac{1}{2} \|f + g - b_l\|_\Sigma^2 + \lambda \|e\|_1 + \|\gamma \cdot d\|_{1,2}$$

$$420 \quad \text{subject to } d = W\chi, \quad e = \mathcal{L}v, \quad f = A\chi, \quad \text{and } g = v.$$

422 Under this reformulation, we summarize the split Bregman algorithm for (2.21) in Algorithm 1.

423 It is easy to see that each subproblem has a closed form solution. The solutions to (2.23)
 424 and (2.24) can be written as

$$425 \quad \chi^{k+1} = (A^T A + I)^{-1} [A^T (f^k - r^k) + W^T (d^k - p^k)] \quad (2.33)$$

$$426 \quad v^{k+1} = (I + \mathcal{L}^T \mathcal{L})^{-1} [g^k - s^k + \mathcal{L}^T (e^k - q^k)]. \quad (2.34)$$

428 Since we use the periodic boundary conditions, both (2.33) and (2.34) can be easily solved by
 429 using the fast Fourier transform. In addition, the solutions to (2.25) and (2.26) are expressed
 430 in terms of the soft thresholding:

$$431 \quad d^{k+1} = \mathcal{T}_{\gamma/\beta}(W\chi^{k+1} + p^k) \quad (2.35)$$

$$432 \quad e^{k+1} = \max(|\mathcal{L}v^{k+1} + q^k| - \lambda/\beta, 0)\text{sign}(\mathcal{L}v^{k+1} + q^k). \quad (2.36)$$

434 Here, \mathcal{T}_γ is the isotropic soft thresholding in [4]: given d defined as

$$435 \quad d = \{d_{l,\alpha} : (l, \alpha) \in (\{0, \dots, L-1\} \times \mathbb{B}) \cup \{(L-1, \mathbf{0})\}\}$$

437 and $\gamma = \{\gamma_l : l = 0, 1, \dots, L-1\}$ with $\gamma_l \geq 0$, $\mathcal{T}_\gamma(d)$ is defined as

$$438 \quad (\mathcal{T}_\gamma(d))_{l,\alpha}[\mathbf{k}] = \begin{cases} d_{l,\alpha}[\mathbf{k}], & (l, \alpha) = (L-1, \mathbf{0}) \\ \max(R_l[\mathbf{k}] - \gamma_l[\mathbf{k}], 0) \frac{d_{l,\alpha}[\mathbf{k}]}{R_l[\mathbf{k}]}, & (l, \alpha) \in \{0, \dots, L-1\} \times \mathbb{B} \end{cases}$$

440 where $R_l[\mathbf{k}] = \left(\sum_{\alpha \in \mathbb{B}} |d_{l,\alpha}[\mathbf{k}]|^2\right)^{1/2}$ for $\mathbf{k} \in \mathbb{O}$. Finally, the solutions to (2.27) and (2.28) are
 441 expressed as

$$442 \quad f^{k+1} = (\Sigma + \beta I)^{-1} [\Sigma(b_l - g^k) + \beta(A\chi^{k+1} + r^k)] \quad (2.37)$$

$$443 \quad g^{k+1} = (\Sigma + \beta I)^{-1} [\Sigma(b_l - f^{k+1}) + \beta(v^{k+1} + s^k)] \quad (2.38)$$

445 where $\Sigma + \beta I$ is simply a diagonal matrix and thus, no matrix inversion is needed.

446 Note that, since our model (2.21) is convex, it can be verified that Algorithm 1 converges
 447 to the minimizer of (2.21) by following the framework of [7, Theorem 3.2.], whenever it has
 448 the unique global minimizer.

449 **3. Experimental Results.** In this section, we present some experimental results on brain
 450 phantom in [54] and in vivo MR data in [52], both of which are available on Cornell MRI
 451 Research Lab webpage¹, to compare the wavelet frame HIRE model (2.21) (Frame-HIRE)
 452 with several existing approaches. In this paper, we choose to compare with the TKD method
 453 (1.5) in [47], the Tikhonov regularization (1.6) in [29], the wavelet frame integral approach
 454 (Frame-Int)

$$455 \quad \min_{\chi \in \mathcal{I}_3} \frac{1}{2} \|A\chi - b_l\|_\Sigma^2 + \|\gamma \cdot W\chi\|_{1,2} \quad (3.1)$$

457 and the wavelet frame differential approach (Frame-Diff)

$$458 \quad \min_{\chi \in \mathcal{I}_3} \frac{1}{2} \|\mathcal{L}A\chi - \mathcal{L}b_l\|_\Sigma^2 + \|\gamma \cdot W\chi\|_{1,2} \quad (3.2)$$

460 where the SNR weight for (3.2) is estimated by the method described in [27]. Moreover, in
 461 order to highlight the main focus of this paper-to propose a two system regularization model

¹<http://www.weill.cornell.edu/mri/pages/qsm.html>

462 by identifying a harmonic incompatibility in the measured local field data, we also test the
 463 models by replacing $\|\gamma \cdot W\chi\|_{1,2}$ in (2.21), (3.1), and (3.2) into the following TGV term:

$$464 \quad \text{TGV}_{\alpha_1, \alpha_0}^2(\chi) = \alpha_1 \|\nabla\chi - p\|_1 + \alpha_0 \|\mathcal{E}p\|_1, \quad \text{where } \mathcal{E} = \frac{1}{2}(\nabla + \nabla^T), \quad (3.3)$$

466 which will be denoted as TGV-HIRE, TGV-Int and TGV-Diff respectively. All experiments
 467 are implemented on MATLAB R2015a running on a platform with 16GB RAM and Intel(R)
 468 Xeon(R) CPU E5-2609 0 at 2.40GHz with 4 cores.

469 In (2.21), (3.1), and (3.2), we choose W to be the tensor product Haar framelet transform
 470 with 1 level of decomposition to avoid the memory storage problem. Note, however, that the
 471 decomposition level and the choice of W will do affect the restoration results. In addition, we
 472 use the standard difference for the TGV term, and the standard centered difference for \mathcal{L} in
 473 the HIRE approaches. The stopping criterion for Algorithm 1 is

$$474 \quad \frac{\|\chi^{k+1} - \chi^k\|_2}{\|\chi^{k+1}\|_2} \leq 5 \times 10^{-3},$$

476 and (3.1) and (3.2) as well as the TGV models are solved using the split Bregman algorithm
 477 presented in [7, 22] with the same stopping criterion as above. For the parameters, we choose γ
 478 in (2.22) as $\gamma = \{\nu 2^{-l} : l = 0, \dots, L-1\}$ with $\nu > 0$ according to [4]. Empirically, we observe
 479 that $\alpha_0 = 2\alpha_1$ for (3.3), $\lambda = 5\nu$ for the Frame-HIRE, and $\lambda = 8\alpha_1$ for the TGV-HIRE are
 480 good choices. Parameters ν and α_1 vary case by case, and are chosen manually to promote
 481 an optimal balance between indices and visual qualities; even though the parameters have
 482 few effects on the indices, the reconstructed images contain more artifacts as the parameters
 483 become smaller. Finally, we compute the root mean square error (RMSE), the structural sim-
 484 ilarity index map (SSIM) [53], and the computation time of the brain phantom experimental
 485 results for the quantitative comparison of each reconstruction model.

486 **3.1. Experiments on Brain Phantom.** For the brain phantom experiments, we use $256 \times$
 487 256×98 image with spatial resolution $0.9375 \times 0.9375 \times 1.5\text{mm}^3$ to simulate the 11 equispaced
 488 multi echo GREs at 3T with TE ranging from 2.6msec to 28.6msec. We first simulate the true
 489 total field by adding four background susceptibility sources in the true susceptibility image to
 490 provide the background field. Then we generate the multi echo complex GRE signal by

$$491 \quad I(\mathbf{k}, t) = \tilde{m}(\mathbf{k}) \exp\{-i\tilde{b}(\mathbf{k})\omega_0 B_0 TE(t)\}, \quad \mathbf{k} \in \mathbb{O}, \ \& \ t = 1, \dots, 11$$

493 with a given true magnitude image \tilde{m} and the true total field \tilde{b} . Then the white Gaussian
 494 noise with standard deviation 0.02 is added to both real and complex part of each GRE signal.
 495 Using the simulated noisy multi echo GRE signal, we estimate the magnitude image and phase
 496 data using the method in [12], and the phase is further unwrapped by the method in [21] to
 497 obtain the noisy and incomplete total field b . Finally, we solve the Poisson's equation (2.10)
 498 using the method in [57] to obtain the noisy local field data b_l . (See Figures 6 and 7.)

499 All regularization based models are initialized with $\chi^0 = 0$, and both the Frame-HIRE
 500 and the TGV-HIRE are also initialized with $v^0 = 0$. For the parameters, we choose $\hbar = 0.125$
 501 for (1.5), $\varepsilon = 0.01$ for (1.6), $\nu = 0.0005$ for the Frame-Int and the Frame-HIRE, $\nu = 0.004$

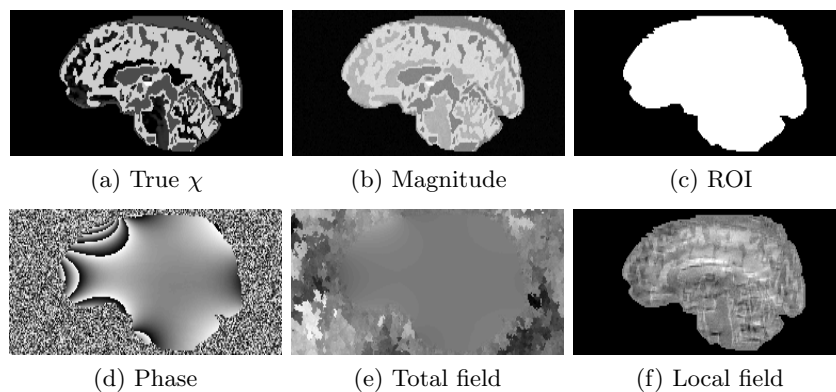


Figure 6. Sagittal slice images of synthesized data sets for the brain phantom experiments.

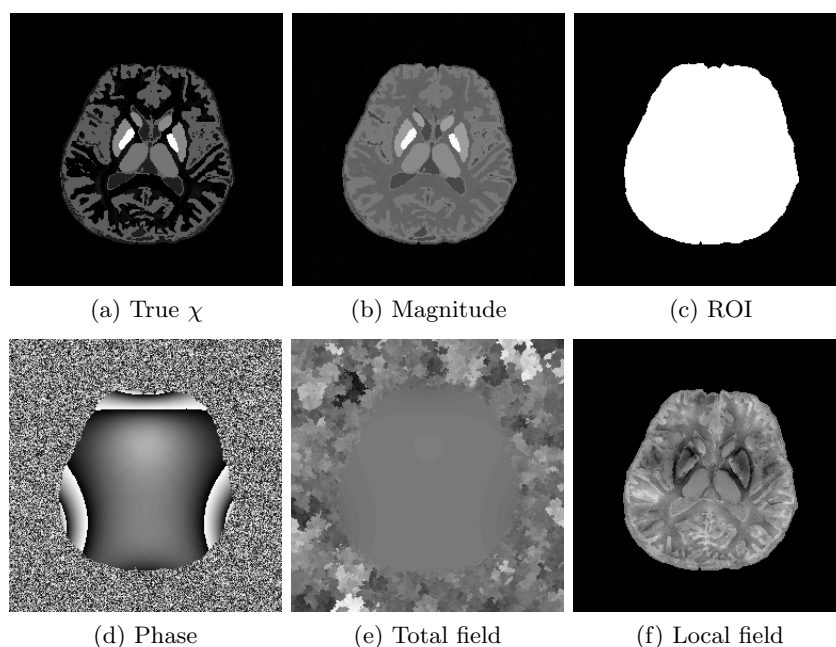


Figure 7. Axial slice images of synthesized data sets for the brain phantom experiments.

502 for the Frame-Diff, $\alpha_1 = 0.00025$ for the TGV-Int and the TGV-HIRE, and $\alpha_1 = 0.002$ for
 503 the TGV-Diff. In addition, we choose $\beta = 0.05$ for all split Bregman algorithms to solve the
 504 regularization based models including [Algorithm 1](#).

505 [Table 1](#) summarizes the relative error and the SSIM of the direct approaches ((1.5) and
 506 (1.6)) and the wavelet frame regularization approaches, and [Figures 8](#) and [9](#) present visual
 507 comparisons of the results. In addition, [Table 2](#) summarizes the aforementioned indices of
 508 the direct approaches and the TGV regularization approaches, and [Figures 10](#) and [11](#) depict
 509 the visual comparisons. We can see that both the Frame-HIRE and the TGV-HIRE consis-
 510 tently outperform the existing direct approaches, the integral approaches, and the differential

Table 1

Comparison of relative error, and structural similarity index map, for the direct approaches and the wavelet frame regularization approach in the brain phantom experiments. The bold-faced numbers indicate the best result.

Indices	Direct Approach		Regularization		
	TKD	Tikhonov	Integral	Differential	HIRE
RMSE	0.5579	0.5546	0.4516	0.6143	0.4183
SSIM	0.6546	0.6474	0.7485	0.6188	0.7586

Table 2

Comparison of relative error, and structural similarity index map for the direct approaches and the TGV regularization approach in the brain phantom experiments. The bold-faced numbers indicate the best result.

Indices	Direct Approach		Regularization		
	TKD	Tikhonov	Integral	Differential	HIRE
RMSE	0.5579	0.5546	0.4129	0.4568	0.3589
SSIM	0.6546	0.6474	0.7861	0.7147	0.7903

511 approaches in both cases. At first glance, this verifies the convention that the regularization
 512 based models in general performs better in solving the ill-posed inverse problem of QSM than
 513 the direct methods [27, 51]. Most importantly, this result demonstrates that the measured
 514 local field data obtained from the phase of a complex GRE MR signal contains the harmonic
 515 incompatibility other than the noise, which agrees with our theoretical discovery, and the
 516 performance gain mainly comes from taking both the noise in the measured data and the
 517 harmonic incompatibility (the incompatibility other than the noise) at the same time. Mean-
 518 while, since this harmonic incompatibility is not taken into account in the integral approaches,
 519 the reconstructed susceptibility images contain the shadow artifacts as shown in [Figures 8d,](#)
 520 [9d, 10d](#) and [11d](#). The differential approaches can remove the harmonic incompatibility in
 521 the measured data in advance, leading to the shadow artifact removal compared to the in-
 522 tegral approach. However, since the noise in b_l was amplified by \mathcal{L} , the final reconstructed
 523 images contain the streaking artifacts as shown in [Figures 8e, 9e, 10e](#) and [11e](#), leading to the
 524 degradation in indices at the same time.

525 Finally, we mention that even though the TGV-HIRE performs slightly better than the
 526 Frame-HIRE from the viewpoint of indices, compared to the Frame-HIRE in [Figures 8f](#) and [9f](#),
 527 the TGV-HIRE yields an overly smoothed restoration results as shown in [Figures 10f](#) and [11f](#).
 528 In addition, since $\mathcal{D}(\mathbf{0}) = 0$, the χ subproblem of the TGV-HIRE has a rank deficient system
 529 matrix due to the constant offset, unlike the Frame-HIRE whose system matrix has a full
 530 column rank due to $W^T W = I$. As a consequence, the CPU time of the TGV-HIRE becomes
 531 approximately 3 times longer than approximately 11.5min of the Frame-HIRE as shown in
 532 [Table 3](#), which shows that the TGV regularization approach may not be suitable for the real
 533 clinical applications. Therefore, even though it is approximately 1.9 times slower than the
 534 Frame-Int, we can nevertheless conclude that compared to the TGV-HIRE, the Frame-HIRE
 535 is able to achieve the efficiency of its split Bregman algorithm as well as the shadow and
 536 streaking artifact removal.

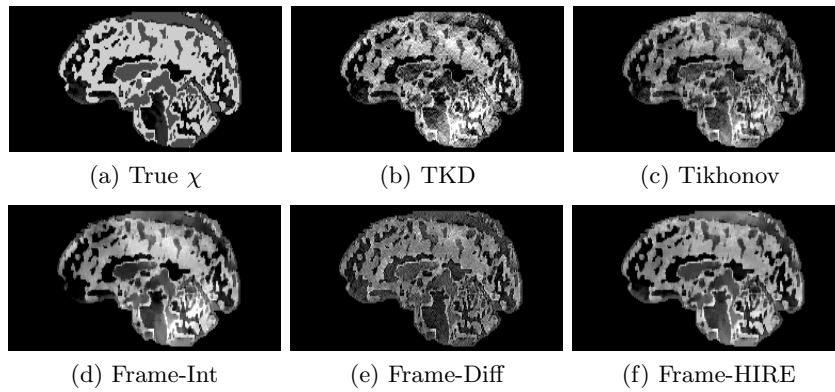


Figure 8. Sagittal slice images comparing QSM reconstruction methods for the brain phantom experiments. All sagittal slice images of brain phantom experimental results are displayed in the window level $[-0.03, 0.07]$ for the fair comparison.

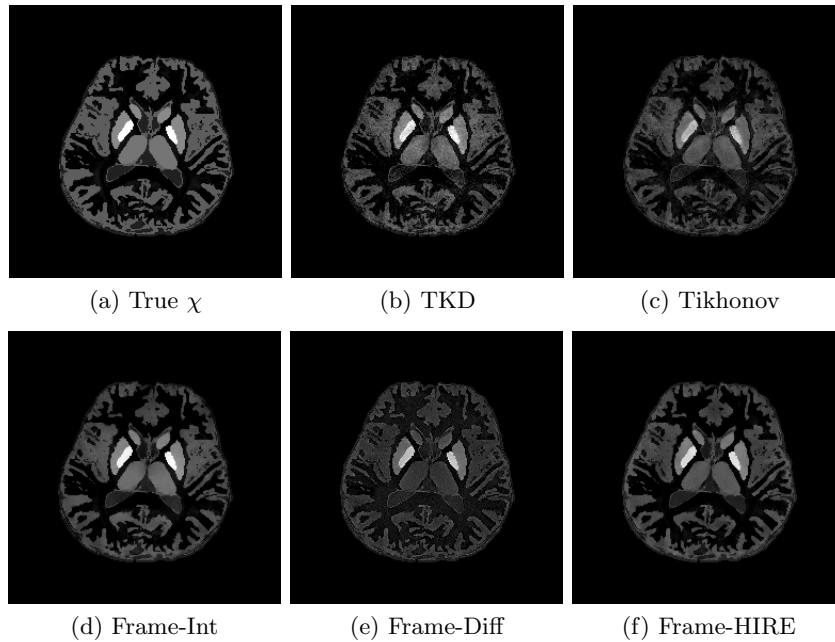


Figure 9. Axial slice images comparing QSM reconstruction methods for the brain phantom experiments with the wavelet frame regularization. All axial slice images of brain phantom experimental results are displayed in the window level $[-0.03, 0.19]$ for the fair comparison.

Table 3

Comparison of the CPU time for the brain phantom w.r.t. the choice of regularization term.

Indices	Wavelet Frame			TGV		
	Integral	Differential	HIRE	Integral	Differential	HIRE
CPU Time	366.55	350.33	685.32	1327.66	365.42	2020.29

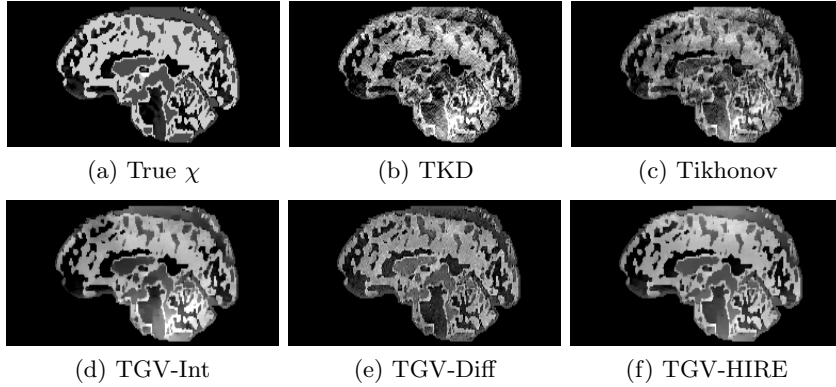


Figure 10. Sagittal slice images comparing QSM reconstruction methods for the brain phantom experiments with the TGV regularization. All sagittal slice images of brain phantom experimental results are displayed in the window level $[-0.03, 0.07]$ for the fair comparison.

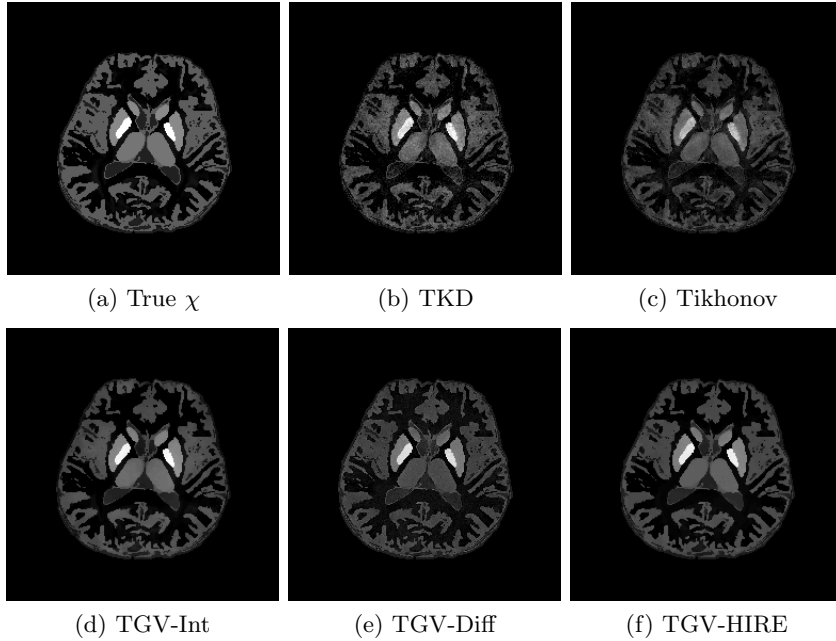
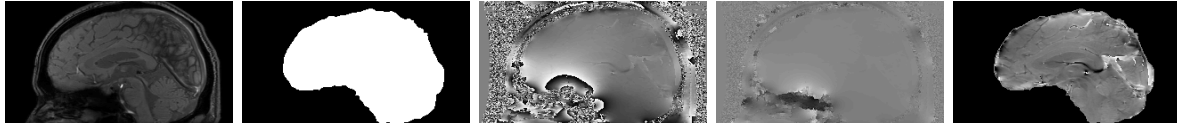


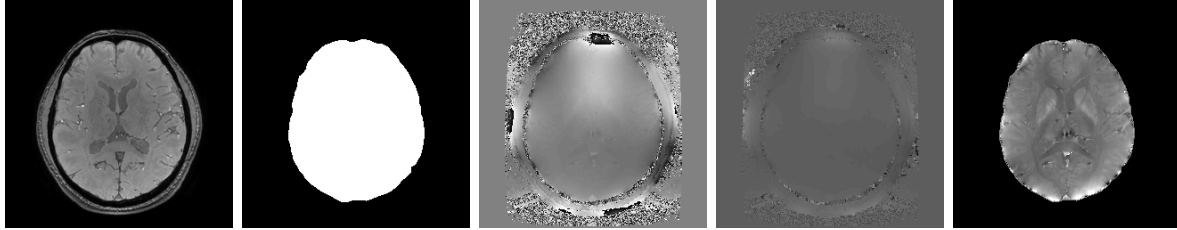
Figure 11. Axial slice images comparing QSM reconstruction methods for the brain phantom experiments with the TGV regularization. All axial slice images of brain phantom experimental results are displayed in the window level $[-0.03, 0.19]$ for the fair comparison.

537 **3.2. Experiments on In Vivo MR Data.** The in vivo MR data experiments are conducted
 538 using $256 \times 256 \times 146$ image with spatial resolution $0.9375 \times 0.9375 \times 1\text{mm}^3$ which can be
 539 downloaded on Cornell MRI Research Lab webpage. Using the wrapped phase image presented
 540 in [Figures 12c](#) and [13c](#), we unwrap the phase using the method in [\[21\]](#) to obtain the total
 541 field b in [Figures 12d](#) and [13d](#) Then the measured local field data b_l in [Figures 12e](#) and [13e](#) is
 542 obtained by solving the Poisson's equation [\(2.10\)](#) using the method in [\[57\]](#).



(a) Magnitude (b) ROI (c) Phase (d) Total field (e) Local field

Figure 12. Sagittal slice images of data sets for the in vivo MR data experiments.



(a) Magnitude (b) ROI (c) Phase (d) Total field (e) Local field

Figure 13. Axial slice images of data sets for the in vivo MR data experiments.

543 As in [subsection 3.1](#), all regularization based models are initialized with $\chi^0 = 0$, and both
 544 the Frame-HIRE and the TGV-HIRE are also initialized with $v^0 = 0$. For the parameters,
 545 we choose $\hbar = 0.1$ for [\(1.5\)](#), $\varepsilon = 0.01$ for [\(1.6\)](#), $\nu = 0.0005$ for the Frame-Int and the Frame-
 546 HIRE, $\nu = 0.005$ for the Frame-Diff, $\alpha_1 = 0.00025$ for the TGV-Int and the TGV-HIRE,
 547 and $\alpha_1 = 0.0025$ for the TGV-Diff. In addition, we choose $\beta = 0.05$ for all split Bregman
 548 algorithms to solve the regularization based models including [Algorithm 1](#).

549 [Figures 14](#) and [15](#) display the visual comparisons of the direct approaches and the wavelet
 550 frame regularization approaches, and the zoom-in views of [Figure 14](#) are provided in [Figure 16](#).
 551 We also provide the visual comparisons of the direct approaches and the TGV regularization
 552 approaches in [Figures 17](#) to [19](#). Since the reference image is not available for in vivo MR data,
 553 it is in general more difficult to provide quantitative evaluations than the numerical brain
 554 phantom. Nonetheless, we can see from the viewpoint of visual comparison that the pros and
 555 cons are almost the same as the numerical brain phantom experiments. It is also worth noting
 556 that the HIRE models can reduce the streaking artifacts which propagate from $\partial\Omega$ into Ω as
 557 well as the shadow artifacts. As pointed out in [\[52\]](#), the in vivo local field data is prone to the
 558 outliers near $\partial\Omega$ because the GRE signal lacks information outside Ω . Hence, we can see that
 559 most streaking artifacts propagate from these outliers near $\partial\Omega$ into the ROI. However, thanks
 560 to the sparsity promoting property of ℓ_1 norm, the term $\lambda \|\mathcal{L}v\|_1$ in the HIRE approaches can
 561 somehow capture and remove them, leading to the suppression of artifacts propagating from
 562 $\partial\Omega$ into Ω as well as the shadow and streaking artifact removal. Finally, even though we can
 563 also note that the Tikhonov regularization can somehow reduce the artifacts, there are some
 564 losses of features due to the smoothness prior of the susceptibility image.

565 Finally, similar to the brain phantom experiments, the TGV-HIRE restores an overly
 566 smoothed susceptibility image as shown in [Figures 17e](#), [18e](#) and [19e](#) compared to the Frame-
 567 HIRE in [Figures 14e](#), [15e](#) and [16e](#). In addition, the split Bregman algorithm of the TGV-HIRE
 568 is approximately 7 times slower than the Frame-HIRE, as shown in [Table 4](#), which again shows

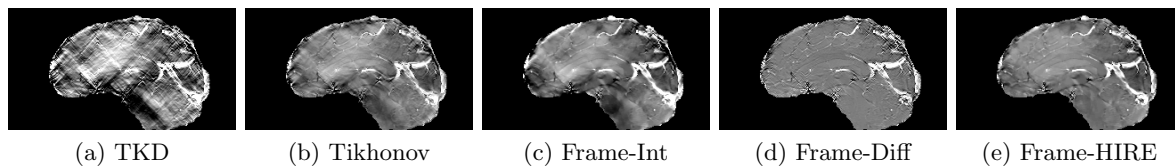


Figure 14. Sagittal slice images comparing QSM reconstruction methods for the *in vivo* MR data experiments with the wavelet frame regularization. All images of *in vivo* MR data experimental results are displayed in the window level $[-0.2, 0.2]$ for the fair comparison.

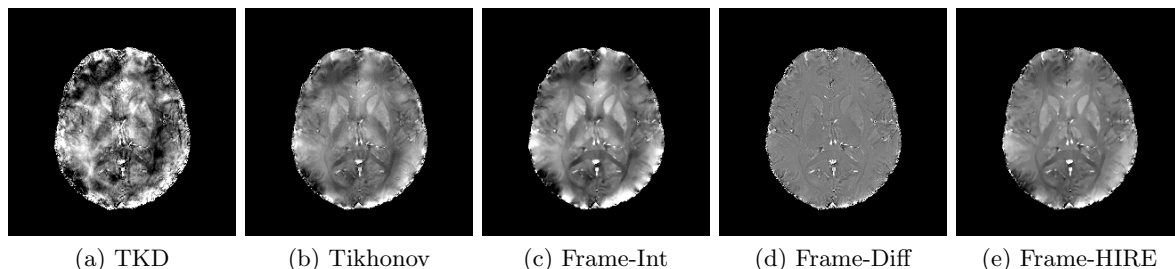


Figure 15. Axial slice images comparing QSM reconstruction methods for the *in vivo* MR data experiments with the wavelet frame Regularization.

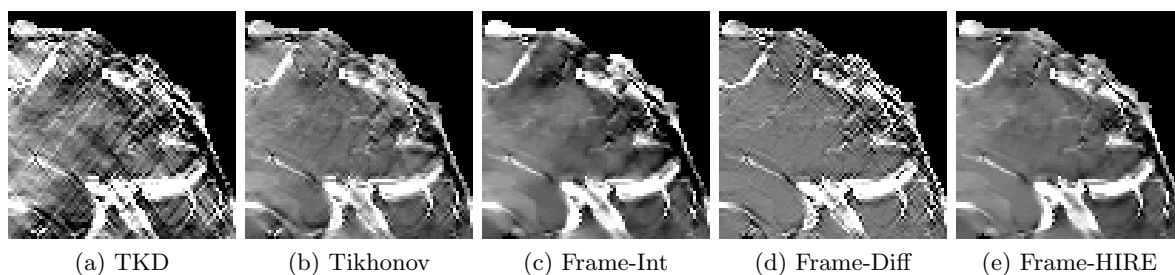


Figure 16. Zoom-in views of [Figure 14](#).

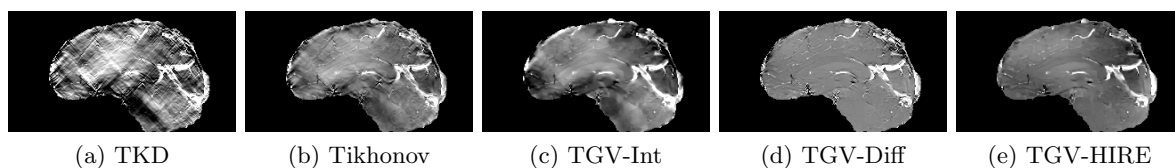


Figure 17. Sagittal slice images comparing QSM reconstruction methods for the *in vivo* MR data experiments with the TGV regularization. All images of *in vivo* MR data experimental results are displayed in the window level $[-0.2, 0.2]$ for the fair comparison.

569 that the TGV regularization approach may not be suitable for the real clinical applications.
 570 Hence, as in the brain phantom experiments, we can conclude that compared to the TGV-
 571 HIRE, the Frame-HIRE is able to achieve the efficiency of its split Bregman algorithm as well
 572 as the shadow and streaking artifact removal.

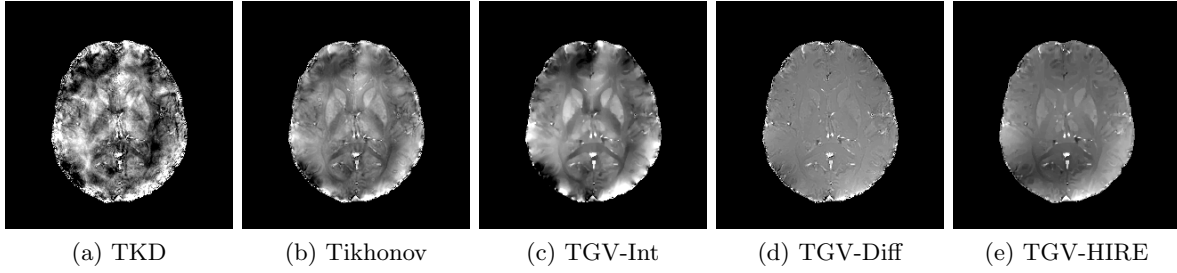


Figure 18. Axial slice images comparing QSM reconstruction methods for the in vivo MR data experiments with the TGV Regularization.

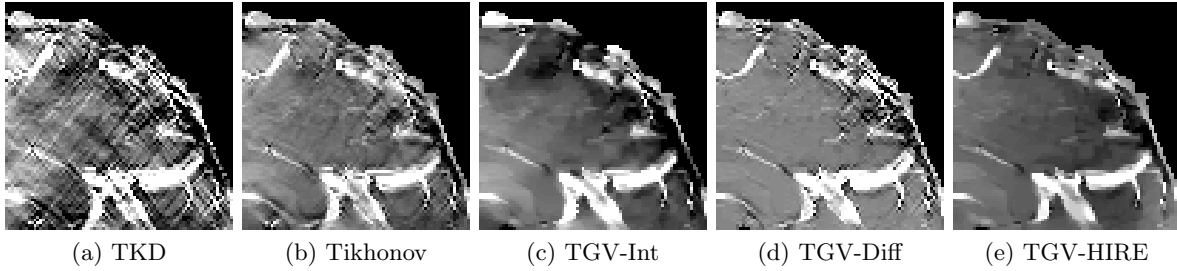


Figure 19. Zoom-in views of Figure 17.

Table 4

Comparison of the CPU time for the in vivo data w.r.t. the choice of regularization term.

Indices	Wavelet Frame			TGV		
	Integral	Differential	HIRE	Integral	Differential	HIRE
CPU Time	628.25	353.32	953.10	3330.51	775.60	6776.12

573 **4. Conclusion.** In this paper, we proposed a new regularization based susceptibility re-
 574 construction model. The proposed HIRE model is based on the identification of the harmonic
 575 incompatibility in the measured local field data arising from the underlying PDE (1.8). The
 576 harmonic property is imposed as a prior of incompatibility via the sparsity under the Lapla-
 577 cian into the integral approach so that we can apply the idea of two system regularization
 578 model. By doing so, we can take the incompatibility in the data which is other than the
 579 additive noise into account, achieving the susceptibility image reconstruction with less arti-
 580 facts. Finally, the experimental results show that our proposed approach (2.21) outperforms
 581 the existing approaches in both brain phantom and in vivo MR data.

582 **Appendix A. Preliminaries on Wavelet Frame.** Provided here is a brief introduction
 583 on the tight wavelet frame. Briefly speaking, it is a generalization of the orthogonal wavelet
 584 basis (e.g. [37]) into the redundant system, and due to the redundancy, it is more robust to
 585 errors than the traditional orthonormal basis [17]. Interested readers may consult [10, 11, 41]
 586 for theories of frame and wavelet frame, [46] for a short survey on the theory and applications
 587 of frames, and [15, 16] for more detailed surveys.

588 For a given $\Psi = \{\psi_1, \dots, \psi_r\} \subseteq L_2(\mathbb{R}^d)$ with $d \in \mathbb{N}$, a quasi-affine system $\mathcal{X}(\Psi)$ generated

589 by Ψ is the collection of the dilations and the shifts of the elements in Ψ :

$$590 \quad \mathcal{X}(\Psi) = \left\{ \psi_{\alpha,n,\mathbf{k}} : 1 \leq \alpha \leq r, n \in \mathbb{Z}, \mathbf{k} \in \mathbb{Z}^d \right\}, \quad (\text{A.1})$$

592 where $\psi_{\alpha,n,\mathbf{k}}$ is defined as

$$593 \quad \psi_{\alpha,n,\mathbf{k}} = \begin{cases} 2^{\frac{nd}{2}} \psi_{\alpha}(2^n \cdot -\mathbf{k}) & n \geq 0; \\ 2^{nd} \psi_{\alpha}(2^n \cdot -2^n \mathbf{k}) & n < 0. \end{cases} \quad (\text{A.2})$$

595 We say that $\mathcal{X}(\Psi)$ is a tight wavelet frame on $L_2(\mathbb{R}^d)$ if we have

$$596 \quad \|f\|_{L_2(\mathbb{R}^d)}^2 = \sum_{\alpha=1}^r \sum_{n \in \mathbb{Z}} \sum_{\mathbf{k} \in \mathbb{Z}^d} |\langle f, \psi_{\alpha,n,\mathbf{k}} \rangle|^2 \quad (\text{A.3})$$

598 for every $f \in L_2(\mathbb{R}^d)$. In this case, each ψ_{α} is called a (tight) framelet, and $\langle f, \psi_{\alpha,n,\mathbf{k}} \rangle$ is called
599 the canonical coefficient of f .

600 The constructions of (anti-)symmetric and compactly supported framelets Ψ are usually
601 based on a multiresolution analysis (MRA); we first find some compactly supported refinable
602 function ϕ with a refinement mask q_0 such that

$$603 \quad \phi = 2^d \sum_{\mathbf{k} \in \mathbb{Z}^d} q_0[\mathbf{k}] \phi(2 \cdot -\mathbf{k}). \quad (\text{A.4})$$

605 Then the MRA based construction of $\Psi = \{\psi_1, \dots, \psi_r\} \subseteq L_2(\mathbb{R}^d)$ is to find finitely supported
606 masks q_{α} such that

$$607 \quad \psi_{\alpha} = 2^d \sum_{\mathbf{k} \in \mathbb{Z}^d} q_{\alpha}[\mathbf{k}] \phi(2 \cdot -\mathbf{k}), \quad \alpha = 1, \dots, r. \quad (\text{A.5})$$

609 The sequences q_1, \dots, q_r are called wavelet frame mask or the high pass filters of the system,
610 and the refinement mask q_0 is also called the low pass filter.

611 The unitary extension principle (UEP) of [41] provides a general theory of the construction
612 of MRA based tight wavelet frames. Briefly speaking, as long as $\{q_0, q_1, \dots, q_r\}$ are compactly
613 supported and their Fourier series $\widehat{q}_{\alpha}(\boldsymbol{\xi}) = \sum_{\mathbf{k} \in \mathbb{Z}^d} q_{\alpha}[\mathbf{k}] e^{-i\boldsymbol{\xi} \cdot \mathbf{k}}$ satisfy

$$614 \quad \sum_{\alpha=0}^r |\widehat{q}_{\alpha}(\boldsymbol{\xi})|^2 = 1 \quad \text{and} \quad \sum_{\alpha=0}^r \widehat{q}_{\alpha}(\boldsymbol{\xi}) \overline{\widehat{q}_{\alpha}(\boldsymbol{\xi} + \boldsymbol{\nu})} = 0 \quad (\text{A.6})$$

616 for all $\boldsymbol{\nu} \in \{0, \pi\}^d \setminus \{\mathbf{0}\}$ and $\boldsymbol{\xi} \in [-\pi, \pi]^d$, the quasi-affine system $\mathcal{X}(\Psi)$ with $\Psi = \{\psi_1, \dots, \psi_r\}$
617 defined by (A.5) forms a tight frame of $L_2(\mathbb{R}^d)$, and the filters $\{q_0, q_1, \dots, q_r\}$ form a discrete
618 tight frame on $\ell_2(\mathbb{Z}^d)$ [15].

619 **Example A.1.** *The piecewise constant B-spline (or the Haar framelet) [11] for $L_2(\mathbb{R})$ has*
620 *one refinable function and one framelet*

$$621 \quad \phi(x) = \begin{cases} 1 & \text{if } x \in [0, 1) \\ 0 & \text{if } x \notin [0, 1) \end{cases} \quad \text{and} \quad \psi_1(x) = \begin{cases} 1 & \text{if } x \in [0, 1/2) \\ -1 & \text{if } x \in [1/2, 1) \\ 0 & \text{if } x \notin [0, 1) \end{cases}$$

622

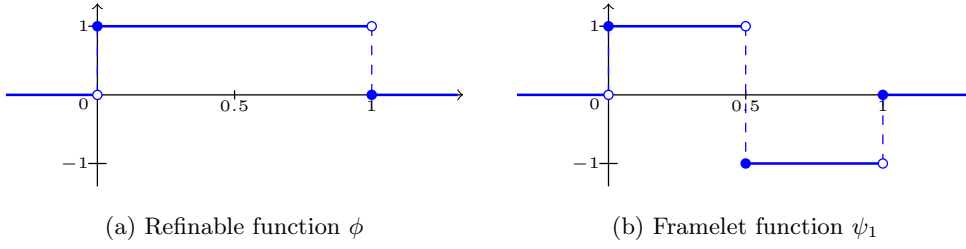


Figure 20. Illustration of ϕ and ψ_1 in Example A.1.

623 as shown in Figure 20. Here, the associated filters are

$$624 \quad q_0 = \frac{1}{2} \begin{bmatrix} 1 & 1 \end{bmatrix} \quad \text{and} \quad q_1 = \frac{1}{2} \begin{bmatrix} 1 & -1 \end{bmatrix}. \quad 625$$

626 Since this $\{q_0, q_1\}$ satisfies (A.6), $\mathcal{X}(\Psi)$ with $\Psi = \{\psi_1\}$ forms a tight frame on $L_2(\mathbb{R})$.

627 The tight frame on $L_2(\mathbb{R}^d)$ with $d \geq 2$ can be constructed by taking tensor products of
 628 univariate tight framelets [4, 5, 10, 15]. Given a set of univariate masks $\{q_0, q_1, \dots, q_r\}$, we
 629 define multivariate masks $q_\alpha[\mathbf{k}]$ with $\alpha = (\alpha_1, \dots, \alpha_d)$ and $\mathbf{k} = (k_1, \dots, k_d) \in \mathbb{Z}^d$ as

$$630 \quad q_\alpha[\mathbf{k}] = q_{\alpha_1}[k_1] \cdots q_{\alpha_d}[k_d], \quad 0 \leq \alpha_1, \dots, \alpha_d \leq r, \quad \mathbf{k} = (k_1, \dots, k_d) \in \mathbb{Z}^d.$$

632 The corresponding multivariate refinable function and framelets are defined as

$$633 \quad \psi_\alpha(\mathbf{x}) = \psi_{\alpha_1}(x_1) \cdots \psi_{\alpha_d}(x_d), \quad 0 \leq \alpha_1, \dots, \alpha_d \leq r, \quad \mathbf{x} = (x_1, \dots, x_d) \in \mathbb{R}^d$$

635 with $\psi_0 = \phi$ for convenience. If the univariate masks $\{q_\alpha\}$ are constructed from UEP, then
 636 we can verify that $\{q_\alpha\}$ satisfies (A.6) and thus $\mathcal{X}(\Psi)$ with $\Psi = \{\psi_\alpha : \alpha \in \{0, \dots, r\}^d \setminus \{\mathbf{0}\}\}$
 637 forms a tight frame for $L_2(\mathbb{R}^d)$.

638 In the discrete setting, let $\mathcal{I}_d \simeq \mathbb{R}^{N_1 \times \dots \times N_d}$ be the space of real valued functions defined on
 639 a regular grid $\{0, 1, \dots, N_1 - 1\} \times \dots \times \{0, 1, \dots, N_d - 1\}$. The fast framelet decomposition,
 640 or the analysis operator with L levels of decomposition is defined as

$$641 \quad Wu = \{W_{l,\alpha}u : (l, \alpha) \in (\{0, \dots, L-1\} \times \mathbb{B}) \cup \{(L-1, \mathbf{0})\}\} \quad (\text{A.7})$$

643 where $\mathbb{B} = \{0, \dots, r\}^d \setminus \{\mathbf{0}\}$ is the framelet band. Then the frame coefficients $W_{l,\alpha}u \in \mathcal{I}_d$ of
 644 $u \in \mathcal{I}_d$ at level l and band α are defined as

$$645 \quad W_{l,\alpha}u = q_{l,\alpha}[-\cdot] \circledast u.$$

647 where \circledast denotes the discrete convolution with a certain boundary condition (e.g. the periodic
 648 boundary condition), and $q_{l,\alpha}$ is defined as

$$649 \quad q_{l,\alpha} = \tilde{q}_{l,\alpha} \circledast \tilde{q}_{l-1,\mathbf{0}} \circledast \cdots \circledast \tilde{q}_{0,\mathbf{0}} \quad \text{with} \quad \tilde{q}_{l,\alpha}[\mathbf{k}] = \begin{cases} q_\alpha[2^{-l}\mathbf{k}], & \mathbf{k} \in 2^l\mathbb{Z}^d \\ 0, & \mathbf{k} \notin 2^l\mathbb{Z}^d. \end{cases} \quad (\text{A.8})$$

650

651 We denote by W^T , the adjoint of W , the fast reconstruction (or the synthesis operator). Then
652 by UEP (A.6), we have $W^T W = I$.

653 Finally, we mention that among many different choice of framelets, the ones constructed
654 from the B-spline are the most popular in image processing. This is due to the multiscale
655 structure of the wavelet frame systems, short supports of the (anti-)symmetric framelet func-
656 tions with varied vanishing moments, and the presence of both low pass and high pass filters
657 in the wavelet frame filter banks, which are desirable in sparsely approximating images [17].
658 A tight frame system constructed from the low order B-spline has fewer filters with shorter
659 supports compared to the ones constructed from the high order B-splines. Hence, low order
660 B-spline framelet systems are more computationally efficient while the high order ones are
661 capable of capturing richer image singularities. Moreover, since high order B-spline framelets
662 have larger supports, they may introduce more numerical viscosity, often leading to smoother
663 reconstructions in image restoration tasks. Hence, the choice of framelet systems indeed de-
664 pends on the the task and the computational cost we can afford [56]. In this paper, we fix W
665 to be the Haar framelet system for the wavelet frame regularization models as the susceptibil-
666 ity images can be well approximated by piecewise constant functions. Besides, we always fix
667 $L = 1$ to avoid the memory storage problem as we solve three dimensional inverse problem.
668 We also note that the choices of W will indeed affect the reconstruction results. For example,
669 the use of data driven tight frames in [6] will generate better reconstruction results due to
670 its adaptivity, even though it requires further numerical studies. Nonetheless, we forgo more
671 details on the choice of W in order not to dilute the main focus of this paper.

672 **Acknowledgments.** The authors thank the authors in [52, 54] for making the data sets and
673 the MATLAB toolbox available so that the experiments can be implemented. The authors
674 also thank the anonymous reviewers for their constructive suggestions and comments that
675 helped tremendously with improving the presentations of this paper.

676

REFERENCES

- 677 [1] J. ACOSTA-CABRONERO, G. B. WILLIAMS, A. CARDENAS-BLANCO, R. J. ARNOLD, V. LUPSON, AND
678 P. J. NESTOR, *In Vivo Quantitative Susceptibility Mapping (QSM) in Alzheimer's Disease*, PloS one,
679 8 (2013), p. e81093, <https://doi.org/10.1371/journal.pone.0081093>.
680 [2] K. BREDIES, K. KUNISCH, AND T. POCK, *Total Generalized Variation*, SIAM J. Imaging Sci., 3 (2010),
681 pp. 492–526, <https://doi.org/10.1137/090769521>.
682 [3] J. F. CAI, R. H. CHAN, AND Z. SHEN, *Simultaneous Cartoon and Texture Inpainting*, Inverse Probl.
683 Imaging, 4 (2010), pp. 379–395, <https://doi.org/10.3934/ipi.2010.4.379>.
684 [4] J. F. CAI, B. DONG, S. OSHER, AND Z. SHEN, *Image Restoration: Total Variation, Wavelet*
685 *Frames, and Beyond*, J. Amer. Math. Soc., 25 (2012), pp. 1033–1089, <https://doi.org/10.1090/S0894-0347-2012-00740-1>.
686 [5] J. F. CAI, B. DONG, AND Z. SHEN, *Image Restoration: a Wavelet Frame Based Model for Piecewise*
687 *Smooth Functions and Beyond*, Appl. Comput. Harmon. Anal., 41 (2016), pp. 94–138, <https://doi.org/10.1016/j.acha.2015.06.009>.
688 [6] J. F. CAI, H. JI, Z. SHEN, AND G. B. YE, *Data-Driven Tight Frame Construction and Image Denoising*,
691 Appl. Comput. Harmon. Anal., 37 (2014), pp. 89–105, <https://doi.org/10.1016/j.acha.2013.10.001>.
692 [7] J. F. CAI, S. OSHER, AND Z. SHEN, *Split Bregman Methods and Frame Based Image Restoration*, Mul-
693 tiscale Model. Simul., 8 (2009/10), pp. 337–369, <https://doi.org/10.1137/090753504>.
694 [8] W. CHEN, S. A. GAUTHIER, A. GUPTA, J. COMUNALE, T. LIU, S. WANG, M. PEI, D. PITT, AND
695 Y. WANG, *Quantitative Susceptibility Mapping of Multiple Sclerosis Lesions at Various Ages*, Radiol-

- 696 ogy, 271 (2014), pp. 183–192, <https://doi.org/10.1148/radiol.13130353>, <https://arxiv.org/abs/https://doi.org/10.1148/radiol.13130353>. PMID: 24475808.
- 697
- 698 [9] J. K. CHOI, H. S. PARK, S. WANG, Y. WANG, AND J. K. SEO, *Inverse Problem in Quantitative Suscep-*
699 *tibility Mapping*, SIAM J. Imaging Sci., 7 (2014), pp. 1669–1689, <https://doi.org/10.1137/140957433>.
- 700 [10] I. DAUBECHIES, *Ten Lectures on Wavelets*, vol. 61 of CBMS-NSF Regional Conference Series in Applied
701 Mathematics, Society for Industrial and Applied Mathematics (SIAM), Philadelphia, PA, 1992, <https://doi.org/10.1137/1.9781611970104>.
- 702
- 703 [11] I. DAUBECHIES, B. HAN, A. RON, AND Z. SHEN, *Framelets: MRA-Based Constructions of Wavelet*
704 *Frames*, Appl. Comput. Harmon. Anal., 14 (2003), pp. 1–46, [https://doi.org/10.1016/S1063-5203\(02\)](https://doi.org/10.1016/S1063-5203(02)00511-0)
705 [00511-0](https://doi.org/10.1016/S1063-5203(02)00511-0).
- 706 [12] L. DE ROCHEFORT, R. BROWN, M. R. PRINCE, AND Y. WANG, *Quantitative MR Susceptibility Mapping*
707 *Using Piece-Wise Constant Regularized Inversion of the Magnetic Field*, Magn. Reson. Med., 60
708 (2008), pp. 1003–1009, <https://doi.org/10.1002/mrm.21710>.
- 709 [13] L. DE ROCHEFORT, T. LIU, B. KRESSLER, J. LIU, P. SPINCEMAILLE, V. LEBON, J. WU, AND Y. WANG,
710 *Quantitative Susceptibility Map Reconstruction from MR Phase Data Using Bayesian Regularization:*
711 *Validation and Application to Brain Imaging*, Magn. Reson. Med., 63 (2010), pp. 194–206, <https://doi.org/10.1002/mrm.22187>.
- 712
- 713 [14] A. V. DIMOV, Z. LIU, P. SPINCEMAILLE, M. R. PRINCE, J. DU, AND Y. WANG, *Bone Quantitative Sus-*
714 *ceptibility Mapping Using a Chemical Species-Specific $R2^*$ Signal Model with Ultrashort and Conven-*
715 *tional Echo Data*, Magn. Reson. Med., 79 (2018), pp. 121–128, <https://doi.org/10.1002/mrm.26648>.
- 716 [15] B. DONG AND Z. SHEN, *MRA-Based Wavelet Frames and Applications*, in Mathematics in Image Pro-
717 cessing, vol. 19 of IAS/Park City Math. Ser., Amer. Math. Soc., Providence, RI, 2013, pp. 9–158.
- 718 [16] B. DONG AND Z. SHEN, *Image Restoration: A Data-Driven Perspective*, in Proceedings of the 8th Interna-
719 tional Congress on Industrial and Applied Mathematics, Higher Ed. Press, Beijing, 2015, pp. 65–108.
- 720 [17] B. DONG, Z. SHEN, AND P. XIE, *Image Restoration: a General Wavelet Frame Based Model and*
721 *Its Asymptotic Analysis*, SIAM J. Math. Anal., 49 (2017), pp. 421–445, [https://doi.org/10.1137/](https://doi.org/10.1137/16M1064969)
722 [16M1064969](https://doi.org/10.1137/16M1064969).
- 723 [18] J. ECKSTEIN AND D. P. BERTSEKAS, *On the Douglas-Rachford Splitting Method and the Proximal Point*
724 *Algorithm for Maximal Monotone Operators*, Math. Programming, 55 (1992), pp. 293–318, <https://doi.org/10.1007/BF01581204>.
- 725
- 726 [19] L. C. EVANS, *Partial differential equations*, vol. 19 of Graduate Studies in Mathematics, American Math-
727 ematical Society, Providence, RI, second ed., 2010, <https://doi.org/10.1090/gsm/019>.
- 728 [20] M. W. GEE, J. J. HU, AND R. S. TUMINARO, *A New Smoothed Aggregation Multigrid Method for*
729 *Anisotropic Problems*, Numer. Linear Algebra Appl., 16 (2009), pp. 19–37, [https://doi.org/10.1002/](https://doi.org/10.1002/nla.593)
730 [nla.593](https://doi.org/10.1002/nla.593).
- 731 [21] D. C. GHIGLIA AND M. D. PRITT, *Two-Dimensional Phase Unwrapping: Theory, Algorithms, and Soft-*
732 *ware*, Wiley-Interscience publication, Wiley, 1998.
- 733 [22] W. GUO, J. QIN, AND W. YIN, *A New Detail-Preserving Regularization Scheme*, SIAM J. Imaging Sci.,
734 7 (2014), pp. 1309–1334, <https://doi.org/10.1137/120904263>.
- 735 [23] E. M. HAACKE, R. W. BROWN, M. R. THOMPSON, AND R. VENKATESAN, *Magnetic Resonance Imaging*
736 *: Physical Principles and Sequence Design*, Wiley, 1st ed., June 1999.
- 737 [24] E. M. HAACKE, S. LIU, S. BUCH, W. ZHENG, D. WU, AND Y. YE, *Quantitative Susceptibility Mapping:*
738 *Current Status and Future Directions*, Magn. Reson. Imaging, 33 (2015), pp. 1 – 25, [https://doi.org/](https://doi.org/https://doi.org/10.1016/j.mri.2014.09.004)
739 <https://doi.org/10.1016/j.mri.2014.09.004>.
- 740 [25] E. M. HAACKE, J. TANG, J. NEELAVALLI, AND Y. C. N. CHENG, *Susceptibility Mapping as a Means*
741 *to Visualize Veins and Quantify Oxygen Saturation*, J. Magn. Reson. Imag., 32 (2010), pp. 663–676,
742 <https://doi.org/10.1002/jmri.22276>.
- 743 [26] Y. KEE, J. CHO, K. DEH, Z. LIU, P. SPINCEMAILLE, AND Y. WANG, *Coherence Enhancement in*
744 *Quantitative Susceptibility Mapping by Means of Anisotropic Weighting in Morphology Enabled Dipole*
745 *Inversion*, Magn. Reson. Med., 79 (2018), pp. 1172–1180, <https://doi.org/10.1002/mrm.26748>.
- 746 [27] Y. KEE, Z. LIU, L. ZHOU, A. DIMOV, J. CHO, L. DE ROCHEFORT, J. K. SEO, AND Y. WANG, *Quantita-*
747 *tive Susceptibility Mapping (QSM) Algorithms: Mathematical Rationale and Computational Imple-*
748 *mentations*, IEEE Trans. Biomed. Eng., 64 (2017), pp. 2531–2545, [https://doi.org/10.1109/TBME.](https://doi.org/10.1109/TBME.2017.2749298)
749 [2017.2749298](https://doi.org/10.1109/TBME.2017.2749298).

- 750 [28] J. KLOHS, A. DEISTUNG, F. SCHWESER, J. GRANDJEAN, M. DOMINIETTO, C. WASCHKIES, R. M.
751 NITSCH, I. KNUESEL, J. R. REICHENBACH, AND M. RUDIN, *Detection of Cerebral Microbleeds with*
752 *Quantitative Susceptibility Mapping in the Arcabeta Mouse Model of Cerebral Amyloidosis*, *J. Cerebr.*
753 *Blood F. Met.*, 31 (2011), pp. 2282–2292, <https://doi.org/10.1038/jcbfm.2011.118>, [https://arxiv.org/](https://arxiv.org/abs/https://doi.org/10.1038/jcbfm.2011.118)
754 [abs/https://doi.org/10.1038/jcbfm.2011.118](https://doi.org/10.1038/jcbfm.2011.118). PMID: 21847134.
- 755 [29] B. KRESSLER, L. DE ROCHEFORT, T. LIU, P. SPINCEMAILLE, J. QUAN, AND Y. WANG, *Nonlinear*
756 *Regularization for Per Voxel Estimation of Magnetic Susceptibility Distributions From MRI Field*
757 *Maps*, *IEEE Trans. Med. Imag.*, 29 (2010), pp. 273–281, <https://doi.org/10.1109/TMI.2009.2023787>.
- 758 [30] W. LI, A. V. AVRAM, B. WU, X. XIAO, AND C. LIU, *Integrated Laplacian-Based Phase Unwrapping and*
759 *Background Phase Removal for Quantitative Susceptibility Mapping*, *NMR in Biomedicine*, 27 (2014),
760 pp. 219–227, <https://doi.org/10.1002/nbm.3056>. NBM-13-0182.R2.
- 761 [31] T. LIU, I. KHALIDOV, L. DE ROCHEFORT, P. SPINCEMAILLE, J. LIU, A. J. TSIOURIS, AND Y. WANG, *A*
762 *Novel Background Field Removal Method for MRI Using Projection onto Dipole Fields (PDF)*, *NMR*
763 *Biomed*, 24 (2011), pp. 1129–1136, <https://doi.org/10.1002/nbm.1670>.
- 764 [32] T. LIU, J. LIU, L. DE ROCHEFORT, P. SPINCEMAILLE, I. KHALIDOV, J. R. LEDOUX, AND Y. WANG,
765 *Morphology Enabled Dipole Inversion (MEDI) from a Single-Angle Acquisition: Comparison with*
766 *COSMOS in Human Brain Imaging*, *Magn. Reson. Med.*, 66 (2011), pp. 777–783, [https://doi.org/10.](https://doi.org/10.1002/mrm.22816)
767 [1002/mrm.22816](https://doi.org/10.1002/mrm.22816).
- 768 [33] T. LIU, P. SPINCEMAILLE, L. DE ROCHEFORT, B. KRESSLER, AND Y. WANG, *Calculation of Susceptibility*
769 *through Multiple Orientation Sampling (COSMOS): A Method for Conditioning the Inverse Problem*
770 *from Measured Magnetic Field Map to Susceptibility Source Image in MRI*, *Magn. Reson. Med.*, 61
771 (2009), pp. 196–204, <https://doi.org/10.1002/mrm.21828>.
- 772 [34] T. LIU, P. SPINCEMAILLE, L. DE ROCHEFORT, R. WONG, M. PRINCE, AND Y. WANG, *Unambiguous*
773 *Identification of Superparamagnetic Iron Oxide Particles through Quantitative Susceptibility Mapping*
774 *of the Nonlinear Response to Magnetic Fields*, *Magn. Reson. Imaging*, 28 (2010), pp. 1383 – 1389,
775 <https://doi.org/https://doi.org/10.1016/j.mri.2010.06.011>.
- 776 [35] T. LIU, C. WISNIEFF, M. LOU, W. CHEN, P. SPINCEMAILLE, AND Y. WANG, *Nonlinear Formulation*
777 *of the Magnetic Field to Source Relationship for Robust Quantitative Susceptibility Mapping*, *Magn.*
778 *Reson. Med.*, 69 (2013), pp. 467–476, <https://doi.org/10.1002/mrm.24272>.
- 779 [36] Z. LIU, P. SPINCEMAILLE, Y. YAO, Y. ZHANG, AND Y. WANG, *MEDI+0: Morphology Enabled Dipole*
780 *Inversion with Automatic Uniform Cerebrospinal Fluid Zero Reference for Quantitative Susceptibility*
781 *Mapping*, *Magn. Reson. Med.*, 79 (2017), pp. 2795–2803, <https://doi.org/10.1002/mrm.26946>, <https://arxiv.org/abs/https://onlinelibrary.wiley.com/doi/pdf/10.1002/mrm.26946>.
782 <https://arxiv.org/abs/https://onlinelibrary.wiley.com/doi/pdf/10.1002/mrm.26946>.
- 783 [37] S. MALLAT, *A Wavelet Tour of Signal Processing, Third Edition: The Sparse Way*, Academic Press,
784 3rd ed., 2008.
- 785 [38] C. MILOVIC, B. BILGIC, B. ZHAO, J. ACOSTA-CABRONERO, AND C. TEJOS, *Fast Nonlinear Sus-*
786 *ceptibility Inversion with Variational Regularization*, *Magn. Reson. Med.*, 80 (2018), pp. 814–821,
787 <https://doi.org/10.1002/mrm.27073>, [https://arxiv.org/abs/https://onlinelibrary.wiley.com/doi/pdf/](https://arxiv.org/abs/https://onlinelibrary.wiley.com/doi/pdf/10.1002/mrm.27073)
788 [10.1002/mrm.27073](https://doi.org/10.1002/mrm.27073).
- 789 [39] F. NATTERER, *Image Reconstruction in Quantitative Susceptibility Mapping*, *SIAM J. Imaging Sci.*, 9
790 (2016), pp. 1127–1131, <https://doi.org/10.1137/16M1064878>.
- 791 [40] B. PALACIOS, G. UHLMANN, AND Y. WANG, *Reducing Streaking Artifacts in Quantitative Susceptibility*
792 *Mapping*, *SIAM J. Imaging Sci.*, 10 (2017), pp. 1921–1934, <https://doi.org/10.1137/16M1096475>.
- 793 [41] A. RON AND Z. SHEN, *Affine Systems in $L_2(\mathbf{R}^d)$: the Analysis of the Analysis Operator*, *J. Funct. Anal.*,
794 148 (1997), pp. 408–447, <https://doi.org/10.1006/jfan.1996.3079>.
- 795 [42] L. I. RUDIN, S. OSHER, AND E. FATEMI, *Nonlinear Total Variation Based Noise Removal Algorithms*,
796 *Phys. D*, 60 (1992), pp. 259–268. *Experimental mathematics: computational issues in nonlinear*
797 *science* (Los Alamos, NM, 1991).
- 798 [43] F. SCHWESER, A. DEISTUNG, B. W. LEHR, AND J. R. REICHENBACH, *Differentiation between Diamag-*
799 *netic and Paramagnetic Cerebral Lesions based on Magnetic Susceptibility Mapping*, *Med. Phys.*, 37
800 (2010), pp. 5165–5178, <https://doi.org/10.1118/1.3481505>.
- 801 [44] F. SCHWESER, A. DEISTUNG., AND J. R. REICHENBACH, *Foundations of MRI Phase Imaging and Pro-*
802 *cessing for Quantitative Susceptibility Mapping (QSM)*, *Zeitschrift für Medizinische Physik*, 26 (2016),
803 pp. 6 – 34, <https://doi.org/https://doi.org/10.1016/j.zemedi.2015.10.002>.

- 804 [45] J. K. SEO, E. J. WOO, U. KATSCHER, AND Y. WANG, *Electro-Magnetic Tissue Properties MRI*, Imperial
805 College Press, London, 1st ed., 2014.
- 806 [46] Z. SHEN, *Wavelet Frames and Image Restorations*, in Proceedings of the International Congress of Math-
807 ematicians. Volume IV, Hindustan Book Agency, New Delhi, 2010, pp. 2834–2863.
- 808 [47] K. SHMUELI, J. A. DE ZWART, P. VAN GELDEREN, T. LI, S. J. DODD, AND J. H. DUYN, *Magnetic*
809 *Susceptibility Mapping of Brain Tissue In Vivo Using MRI Phase Data*, Magn. Reson. Med., 62
810 (2009), pp. 1510–1522, <https://doi.org/10.1002/mrm.22135>.
- 811 [48] E. M. STEIN AND R. SHAKARCHI, *Functional Analysis. Introduction to Further Topics in Analysis*, vol. 4
812 of Princeton Lect. Anal., Princeton University Press, Princeton, NJ, 2011.
- 813 [49] J. TANG, S. LIU, J. NEELAVALLI, Y. C. N. CHENG, S. BUCH, AND E. M. HAACKE, *Improving Suscep-*
814 *tibility Mapping Using a Threshold-Based k -space/Image Domain Iterative Reconstruction Approach*,
815 Magn. Reson. Med., 69 (2013), pp. 1396–1407, <https://doi.org/10.1002/mrm.24384>.
- 816 [50] J. M. G. VAN BERGEN, J. HUA, P. G. UNSCHULD, I. A. L. LIM, C. K. JONES, R. L. MARGOLIS, C. A.
817 ROSS, P. C. M. VAN ZIJL, AND X. LI, *Quantitative Susceptibility Mapping Suggests Altered Brain*
818 *Iron in Premanifest Huntington Disease*, Amer. J. Neuroradiol, 37 (2016), pp. 789–796, <https://doi.org/10.3174/ajnr.A4617>, <https://arxiv.org/abs/http://www.ajnr.org/content/37/5/789.full.pdf>.
- 820 [51] S. WANG, T. LIU, W. CHEN, P. SPINCEMAILLE, C. WISNIEFF, A. J. TSIOURIS, W. ZHU, C. PAN,
821 L. ZHAO, AND Y. WANG, *Noise Effects in Various Quantitative Susceptibility Mapping Methods*,
822 IEEE Trans. Biomed. Eng., 60 (2013), pp. 3441–3448, <https://doi.org/10.1109/TBME.2013.2266795>.
- 823 [52] Y. WANG AND T. LIU, *Quantitative Susceptibility Mapping (QSM): Decoding MRI Data for a Tissue*
824 *Magnetic Biomarker*, Magn. Reson. Med., 73 (2015), pp. 82–101, <https://doi.org/10.1002/mrm.25358>.
- 825 [53] Z. WANG, A. C. BOVIK, H. R. SHEIKH, AND E. P. SIMONCELLI, *Image Quality Assessment: from*
826 *Error Visibility to Structural Similarity*, IEEE Trans. Image Process., 13 (2004), pp. 600–612, <https://doi.org/10.1109/TIP.2003.819861>.
- 828 [54] C. WISNIEFF, T. LIU, P. SPINCEMAILLE, S. WANG, D. ZHOU, AND Y. WANG, *Magnetic Susceptibility*
829 *Anisotropy: Cylindrical Symmetry from Macroscopically Ordered Anisotropic Molecules and Accuracy*
830 *of MRI Measurements Using Few Orientations*, NeuroImage, 70 (2013), pp. 363 – 376, <https://doi.org/https://doi.org/10.1016/j.neuroimage.2012.12.050>.
- 832 [55] F. YANEZ, A. FAN, B. BILGIC, C. MILOVIC, E. ADALSTEINSSON, AND P. IRARRAZAVAL, *Quantita-*
833 *tive Susceptibility Map Reconstruction via a Total Generalized Variation Regularization*, in 2013
834 International Workshop on Pattern Recognition in Neuroimaging, June 2013, pp. 203–206, <https://doi.org/10.1109/PRNI.2013.59>.
- 836 [56] H. ZHANG, B. DONG, AND B. LIU, *A Reweighted Joint Spatial-Radon Domain CT Image Reconstruction*
837 *Model for Metal Artifact Reduction*, SIAM J. Imaging Sci., 11 (2018), pp. 707–733, <https://doi.org/10.1137/17M1140212>.
- 839 [57] D. ZHOU, T. LIU, P. SPINCEMAILLE, AND Y. WANG, *Background Field Removal by Solving the Laplacian*
840 *Boundary Value Problem*, NMR in Biomedicine, 27 (2014), pp. 312–319, <https://doi.org/10.1002/nbm.3064>. NBM-13-0115.R3.
- 841